

Experimental investigations of atomization characteristics of an airblast atomizer at high ambient pressure

by

Zichen Zhang

A thesis submitted to the graduate faculty
in partial fulfillment of the requirements for the degree of

MASTER OF SCIENCE

Major: Aerospace Engineering

Program of Study Committee:

Hui Hu, Major Professor

Thomas Ward

Juan Ren

The student author, whose presentation of the scholarship herein was approved by the program of study committee, is solely responsible for the content of this thesis. The Graduate College will ensure this thesis is globally accessible and will not permit alterations after a degree is conferred.

Iowa State University

Ames, Iowa

2020

Copyright © Zichen Zhang, 2020. All rights reserved.

TABLE OF CONTENTS

	Page
LIST OF FIGURES	iii
NOMENCLATURE	vi
ACKNOWLEDGMENTS	viii
ABSTRACT.....	ix
CHAPTER 1. GENERAL INTRODUCTION	1
CHAPTER 2. RESEARCH METHODOLOGY	8
High-pressure Spray Test Facility	8
Stereo Particle Image Velocimetry	12
CHAPTER 3. MEASUREMENT RESULTS AND DISCUSSION	19
Effects of Pressure Drop Ratio on Spray Characteristics	19
Effects of Ambient Pressure on Spray Characteristics	34
Effects of Liquid Flow Rate on Spray Characteristics	45
CHAPTER 4. CONCLUSION.....	50
REFERENCES	52
APPENDIX A. LIST OF TEST CASES	57
APPENDIX B. SUMMARY OF MEASUREMENT RESULTS OF SPRAY FLOWS	58

LIST OF FIGURES

	Page
Figure 2-1. (a). A photograph of the high-pressure test facility and one of the specially-designed rotating window; (b). Schematic of the high-pressure test facility.	9
Figure 2-2. Structure of the airblast atomizer investigated in the present study.	10
Figure 2-3. The schematic diagram of data acquisition units.	11
Figure 2-4. A typical acquired data of pressure and temperature during the experiment.	11
Figure 2-5. (a). The principle of stereoscopic imaging; (b). An example of two cameras views for SPIV measurement.	14
Figure 2-6. Schematic diagram showing the reconstruction of three-dimensional displacement vectors of tracer particles using displacement vectors recorded by two cameras.	16
Figure 2-7. Schematic diagram of SPIV setup and the photograph of SPIV setup on the high-pressure test facility at Iowa State University.	17
Figure 3-1. Smoke particle images taken by two different cameras for the SPIV measurement at an ambient pressure of 105 psi and a pressure drop ratio of 2%.	19
Figure 3-2. Time-averaged velocity vector fields of air at an ambient pressure of 15 psi with different pressure drop ratios: (a) 2%, (b) 4% and (c) 6%. The profile of velocity magnitude of air at three different locations: (d) $Y = 12.7$ mm, (e) $Y = 25.4$ mm and (f) $Y = 35.1$ mm.	21
Figure 3-3. Turbulence kinetic energy and a Reynolds stress component with vertical and azimuthal velocity fluctuation (v' and w') at an ambient pressure of 15 psi with pressure drop ratios: (a) and (f) 2%, (b) and (e) 4%, (c) and (d) 6%.	23
Figure 3-4. Normalized time-averaged velocity fields of air at an ambient pressure of 15 psi with different pressure drop ratios: (a) 2%, (b) 4% and (c) 6%. The profiles of normalized velocity at locations: (d) $Y = 12.7$ mm, (e) $Y = 25.4$ mm and (f) $Y = 35.1$ mm.	28
Figure 3-5. A typical image pair of spray droplets for SPIV measurements.	29

Figure 3-6. (a) <i>The time-averaged velocity vector field and color map of spray droplets at an ambient pressure of 15 psi with a pressure drop ratio of 4%. (b) The velocity profile at $Y = 25.4$ mm of spray droplets and air.</i>	30
Figure 3-7. <i>Stokes number of droplets with different diameters.</i>	33
Figure 3-8. <i>Time-averaged airflow velocity fields at a pressure drop ratio of 4% with ambient pressures: (a) 35 psi and (b) 105 psi. The profiles of velocity magnitude at two different locations: (c) $Y = 12.7$ mm and (d) $Y = 38.1$ mm.</i>	34
Figure 3-9. <i>Time-averaged air velocity vector fields at a pressure drop ratio of 4% with ambient pressures: (a) 35 psi and (b) 105 psi. The profiles of velocity magnitude at two different locations: (c) $Y = 12.7$ mm and (d) $Y = 38.1$ mm.</i>	35
Figure 3-10. <i>Time-averaged air velocity vector fields at a pressure drop ratio of 6% with ambient pressures: (a) 35 psi and (b) 105 psi. The profile of velocity magnitude at two different locations: (c) $Y = 12.7$ mm and (d) $Y = 38.1$ mm.</i>	36
Figure 3-11. <i>Time-averaged velocity vector fields of spray flow at a pressure drop ratio of 4% with ambient pressures: (a) 35 psi and (b) 105 psi. The profiles of velocity magnitude at two different locations: (c) $Y = 12.7$ mm and (d) $Y = 38.1$ mm.</i>	39
Figure 3-12. <i>Velocity profiles of air and spray droplets at a pressure drop ratio of 4% with ambient pressures: (a, b) 15 psi, (c, d) 35 psi and (e, d) 105 psi at two different locations: $Y = 12.7$ mm and $Y = 38.1$ mm.</i>	40
Figure 3-13. <i>Effects of ambient pressure on tracing capacity of spray droplets at ambient pressure: 15 psi (cycle), 35 psi (triangle), and 105 psi (cross).</i>	44
Figure 3-14. <i>Illuminated spray droplets by a laser sheet with a pressure drop ratio of 4% under different ambient pressures: (a) 15 psi, (b) 35 psi and (c) 105 psi.</i>	45
Figure 3-15. <i>Spray droplets at a pressure drop ratio of 4% with ambient pressures of 105 psi (a, b), 35 psi (c, d) and 15 psi (e, f) and flow rates 24 ml/min (a, c, e) and 90 ml/min (b, d, f).</i>	47
Figure 3-16. <i>Velocity profiles of air and spray flow at a pressure drop ratio of 4% with an ambient pressure 15 psi and flow rates of 24 ml/min and 90 ml/min at two different locations: (a) $Y = 12.7$ mm and (b) $Y = 38.1$ mm.</i>	48
Figure 3-17. <i>Velocity profiles of air and spray flow at a pressure drop ratio of 4% with an ambient pressure 35 psi and flow rates of 24 ml/min and 90 ml/min at two different locations: (a) $Y = 12.7$ mm and (b) $Y = 38.1$ mm.</i>	48

- Figure 3-18. *Velocity profiles of air and spray flow at a pressure drop ratio of 4% with an ambient pressure 105 psi and flow rates of 24 ml/min and 90 ml/min at two different locations: (a) $Y = 12.7$ mm and (b) $Y = 38.1$ mm. 49*
- Figure B-1. *Time-averaged velocity fields of spray flow at a pressure drop ratio of 2% with an ambient pressure 105 psi and flow rates of (a). 20 ml/min, 68 ml/min and (c). 110 ml/min. 58*
- Figure B-2. *Time-averaged velocity vector fields of spray flow at a pressure drop ratio of 3% with an ambient pressure 105 psi and liquid flow rates of (a). 22 ml/min and (b). 79 ml/min. 58*
- Figure B-3. *Time-averaged velocity vector fields of spray flow at a pressure drop ratio of 4% with an ambient pressure 15 psi and liquid flow rates of (a). 4.7 ml/min, (b) 24.4 ml/min, (c) 39.2 ml/min, (d) 54.7 ml/min and (e). 91 ml/min. 59*
- Figure B-4. *Time-averaged velocity vector fields of spray flow at a pressure drop ratio of 4% with an ambient pressure 15 psi and liquid flow rates of (a). 10.0 ml/min, (b) 24.5 ml/min, (c) 69.5 ml/min, (d) 90.7 ml/min, (e). 113.5 ml/min and (f). 148.2 ml/min. 60*

NOMENCLATURE

C_d	Drag Coefficient
C_p	Specific Heat at Constant Pressure
d_p	Particle Diameter
D	Drag of a Particle
e	Internal Energy
f	Body Force
h	Enthalpy
I	Image Intensity
l	Reference Length
M	Mach Number
P	Ambient Pressure
PDPA	Phase Doppler Particle Analyzer
$\Delta P\%$	Relative Pressure Drop Ratio
PIV	Particle Image Velocimetry
\dot{q}	Heat Flux
r	Cross-correlation Coefficient
R	Specific Gas Constant
Re	Reynolds Number
SPIV	Stereoscopic Particle Image Velocimetry
S	Entropy
Stk	Stokes Number
t	Time

t_0	Characteristic Response Time
Δt	Time Duration
T	Temperature
TKE	Turbulence Kinetic Energy
u', v', w'	Three Components of Velocity Fluctuation
V	Velocity Magnitude
V_c	Characteristic Velocity
\mathbf{V}	Velocity Vector
W	Azimuthal Velocity
x, y, z	Spatial Coordinates
$\Delta x, \Delta y, \Delta z$	Three Components of Particle Displacement
α, β	View Angles
γ	Heat Capacity Ratio
μ	Dynamic Viscosity
μ_g	Gas Dynamic Viscosity
v	Specific Volume
ρ	Air Density
ρ_p	Particle Density
τ	Shear Stress
τ_R	Reynolds Stress

ACKNOWLEDGMENTS

I would like to thank my committee chair, Hui Hu, and my committee members, Thomas Ward and Juan Ren, for their guidance and support throughout the course of this research and for the insightful comments and suggestions on this research.

Besides, I would also like to thank my colleagues in our lab: Dr. Wenwu Zhou, Dr. Haixing Li, Dr. Pavithra Premaratne, Dr. Zhe Ning, Dr. Linkai Li, Dr. Linyue Gao, Dr. Cem Kolbakir, Ramsankar Veerakumar, Haiyang Hu, Linchuan Tian, Nianhong Han, Ahmad Siddique, Faisal Al-Masri, Prashanth Sagar and Abigayle Moser for the fruitful discussion. I would like to thank all the staff members in the Department of Aerospace Engineering, especially laboratory associate Andrew Jordan and graduate program assistant Mendoza Marisa for making my time at Iowa State University a wonderful experience.

Thank you to the project sponsor Collins Aerospace Company for the support.

Thank you very much Bin, Haoran, and Yan for great discussions about career, life and research. Thank you Wenting.

Thank you very much Liqun and Yang for providing great assistance for my research and life.

Finally, and most importantly, I would like to express my deepest appreciation to my parents for their support and love.

ABSTRACT

Spray performance of swirling airblast atomizer is important to fuel droplet combustion, heat transfer and pollutant emission for aircraft engines. Optimizing atomization characteristics of fuel injectors is one of goal for next generation aircraft. A comprehensive experimental investigation motivated by improving the efficiency of aircraft engines and reducing pollutant emissions was performed in a high-pressure spray test facility which is built in Iowa State University to study spray characteristics of an airblast atomizer under different working conditions. The effects of pressure drop ratio, ambient pressure, and fuel flow rate on spray characteristics and fuel injector performance are studied using stereo particle image velocimetry (SPIV). It was found that while air velocity fields can be significantly affected by the pressure drop ratio, the influences of ambient pressure is very slightly. Furthermore, a theoretical analysis reveals that if the airflow is assumed to be isentropic, inviscid and steady, airflow velocity should be proportional to the square root of the pressure drop ratio. At atmospheric pressure, the flow field at various pressure drop ratios can satisfy it very well but under high ambient pressure (e.g., 105 psi), the velocity magnitude is not perfectly proportional to the pressure drop ratio. Next, it should be noted that both ambient pressure and pressure drop ratio can greatly affect the spray velocity field. Spray droplets can obtain a higher velocity with a larger ambient pressure or a higher pressure drop ratio. Furthermore, the velocity profile of spray droplets gradually approaches the airflow velocity profile as ambient pressure is increasing. This phenomenon indicates the tracing capacity of spray droplets is getting better at high ambient pressures. A theoretical model is built to show the effects of ambient pressure on the droplets tracing capacity by evaluating Stokes number of droplets under different ambient pressures. The analysis suggests that at high ambient pressure, Stokes number for droplets significantly gets smaller (i.e. better tracing capacity) due to the increase of air density.

It reveals that droplets seem more possible to closely follow air stream motion under high ambient pressure. In addition, the shrinking size of droplets at high ambient pressure also provides better tracing capacity for droplets. These results and analysis suggest that future studies about fuel atomization should be conducted under high ambient pressure (e.g., >100 psi), since the airblast atomizer may have distinctive performance under different ambient pressures. Finally, the effects of the liquid flow rate on the spray velocity field are found to be very slight. When liquid flowrate increases from 24 ml/min to 90 ml/min, the velocity magnitude of spray droplets gets a little smaller due to the increase of the number of liquids but this change is within 5 m/s. This result shows the stable performance of the airblast atomizer under different operating conditions.

CHAPTER 1. GENERAL INTRODUCTION

The fuel atomization systems play an important factor in improving performance of modern aircraft engines because they significantly affect the breakup, vaporization and evaporation process as well as velocity and motion trajectories of liquid fuels in the combustor before igniting fuel droplets. The fuel atomizer is one of the most essential part of atomization systems for aircrafts. A good design of fuel injector/atomizer highly reduces the greenhouse gas emission, enhances fuel efficiency and provides higher reliability and security to the aircraft [1–3]. There are plenty of atomizers designed for different applications such as pressure atomizer, simplex atomizer, effervescent atomizer, rotary atomizer, plasma atomizer, airassist atomizer and airblast atomizer [4–7]. However, pressure atomizer, rotary atomizer, and airblast atomizer are three most widely used atomizers. The atomization process of pressure atomizer is achieved by discharging the liquid at high velocity or high pressure into the surrounding quiescent air [8]. Plain-orifice atomizer is a typical pressure atomizer and is widely used in diesel, rocket and turbojet engines due to its simplicity and ease of manufacture. But its spray cone angle of it is relatively narrow (i.e. $\sim 10^\circ$), which might affect combustion process [9]. Adding a swirl chamber or a spin chamber in the front of the plain-orifice atomizer could overcome this problem by spreading fuel radially outward to form a hollow conical spray whose cone angles could reach up to 30° . The pressure atomizer with such configuration is usually called simplex atomizer. As the liquid flow rate is doubled for the plain-orifice atomizer and simplex atomizer, it requires a fourfold increase in injection pressure, which significantly restricts the application of this kind of atomizers due to practical limits on injection pressure [10]. The invention of dual-orifice atomizer attempts to resolve this drawback by fitting one orifice atomizer concentrically inside the other to increase the flow rate without an extra increase of injection pressure. Besides pressure atomizers, rotary

atomizers, which utilize the centrifugal force to break up the liquid ligaments, can also achieve good atomization results. More specifically, when a liquid is injected at the center over the surface of a rotating disc, it radially moves outward to the periphery where liquid ligaments are formed and then, break up in the form of droplets of fairly uniform size due to the Plateau-Rayleigh instability. Airblast atomizers utilize the kinetic energy of a high-speed airstream to break liquid jets or sheets into spray droplets, which increases the mixing rate of air and fuel and evaporation rate of fuel droplets [11]. In addition to the lower operating pressure, the spray generated by airblast atomizer is characterized by fine quality and uniform size, and the atomization process of airblast atomizer is characterized by thorough mixing of fuel drops and air. High-speed airflow is used either to break liquid sheets or to deflect the droplets radially outward to create a spray cone. Recently, airblast atomizers have been widely used in aircraft engines because they require lower supplying air pressure, have high fuel-air mixing ratio, and generate good-quality fuel sprays. The atomizer which was investigated in the present study is an airblast atomizer and more specifically, it is a swirling prefilming airblast atomizer. However, it should be noted that the performance of airblast atomizers is affected by multiple factors such as supplying air pressure, rate of fuel flow, ambient pressure, temperature, atomizer geometry, fuel viscosity, fuel viscoelasticity and fuel surface tension. Hence, several studies have been conducted to find the optimal operating conditions of airblast atomizers for different fuels [9,12–27].

One way to characterize the performance of an airblast atomizer is measuring the average size or Sauter-mean-diameter (SMD) of spray droplets since droplet size distribution significantly affect the droplet evaporation rate and combustion efficiency of fuels. Phase Doppler particle analyzer (PDPA) and shadowgraph technique are often used to quantify the droplet size. Rizkalla and Lefebvre [14] found that for a swirling airblast atomizer, the SMD of spray droplets is smaller

with higher air velocity, and SMD is inversely proportional to the air velocity. Lorenzetto and Lefebvre [28] also proposed that a decrease in the size of spray droplets can be achieved by raising air velocity for airblast atomizers; they even claimed that air velocity undoubtedly is the most important factor influencing droplet size in the spray. Then, Rizk and Lefebvre [29] confirmed the research conclusion that the size of spray droplets decreases as air velocity rises after testing different airblast atomizers. They also identified that the uniformity of droplets size in the spray increases when average droplet size is reduced, which is beneficial to improving the fuel combustion efficiency. Besides air velocity, design features of airblast atomizers also play an important role in average droplet size and droplet size distribution. Rizk and Lefebvre [16] recognized that minimizing the angle enclosed by the liquid jet and the airstream can reduce the SMD of spray droplet for plain-jet airblast atomizers so that liquid jets/sheets should be surrounded by coaxial streams of air to improve the performance of atomizers. Harani and Sher [30] showed that the most uniform droplet distribution is obtained when angle of impact between the air jet and the liquid jet is 30° . Recently, the design and optimization of airblast atomizer geometry highly relies upon high-accuracy numerical simulations to shorten the research time and to reduce research expenses [31,32]. Additionally, physical properties of fuels also greatly affect the size of spray droplets in fuel spray. For example, for a given air velocity, fuel flow rate and ambient pressure, the mean droplet size of the liquid spray generated by an airblast atomizer increases with the increase in liquid viscosity, surface tension and liquid density [14]. The increase in the viscosity and surface tension of liquids fuels augments the forces resisting the breakup of liquid jets/sheets into spray droplets so that the average droplet size of a more viscous liquid fuel is larger [33]. Mansour and Chigier [34] found that viscoelastic liquids are much more difficult to atomize

compared to Newtonian fluids because the large normal stress developed in viscoelastic materials inhibits the breakup of liquid jets/sheets and large droplets.

The performance of airblast atomizers can also be characterized by spray angle, penetration depth and droplets velocity using flow visualization techniques such high-speed imaging system and laser-based advanced flow diagnostic techniques. Extensive studies have been conducted to investigate these physical parameters because fuel combustion efficiency and flame propagation in the combustor of engines are strongly affected by them [22,35,36]. It was found that the spray angle is not sensitive to the liquid flow rate for many airblast atomizers, but it can be substantially affected by supplying air pressure [37]. Gad et al. [38] confirmed that the design feature of airblast atomizer (e.g., atomizing air swirler angle and atomizing air exit orifice) can also affect the spray angle as well as the droplets spatial density. While the increase of atomizing air swirler angle leads to the rise of spray angle, the spray angle reduces when atomizing air exit orifice is increasing. Kim et al. [36] associated the spray angle to Weber number, and they proposed that spray angle increases as the Weber number increases before the break up of liquid sheets. Leong et al. [20] reported the increase of spray penetration depth as air pressure drop rises. Furthermore, the quantitative measurement of the droplets velocity or airflow velocity is very useful to understand the underlying physics of the interaction between spray droplets and airstreams during the atomization process. The particle velocity in the flow field can usually be measured by PDPA and particle image velocimetry (PIV). PDPA is a technique of using the Doppler shift in a laser beam to measure the velocity of particles in fluid flows but it can only measures the velocity at a point. PIV is a technique for quantifying instantaneous velocity and related properties in fluid flows using visible tracer particles and laser illumination; it can produce two-dimensional or three-dimensional velocity fields. Merkle et al. [39] used PDPA to measure the flow field of airblast atomizers with

co-swirl and counter-swirl configurations, and they found that the co-swirl arrangement has faster mixing rate of fuel and air. Batarseh et al. [40] applied PDPA technique and high-speed video system to study the frequencies of velocity fluctuation and shape fluctuation of spray flow, and they noticed that both fluctuations have the same frequency over a wide range of spray parameters. Rajamanickam and Basu [23] applied time-resolved PIV and high-speed imaging techniques to explore the interaction between liquid sheets and airstreams. Based on their results, they prove the existence of Kelvin-Helmholtz instability mechanism in the breakup of liquid sheets with the assistance of proper orthogonal decomposition [24]. Rajamanickam and Basu [25] also stated that the outer shear layer is dominated by shedding mode coupling in addition to the Kelvin-Helmholtz instability, whereas inner shear flow is only dominated by Kelvin-Helmholtz mode. PIV technique was combined with dynamic mode decomposition method to explore the basic flow mode of jet flow, which helps to understand the disintegration of liquid jets in the atomization process [41]. While the influence of external physical environment (e.g., supplying air pressure and atomizer geometry) and physical properties of fuels (e.g., fuel viscosity) has been widely investigated, the effect of ambient pressure on fuel atomization has been often ignored because many studies of airblast atomizers were conducted at atmospheric pressure (i.e. 10^5 Pa) or in an open chamber.

The effects of ambient pressure on the performance of atomizers have been investigated by some previous studies [14,19,20,36,42,43]. Jasuja [19] stated that mean velocity of spray droplets diminishes with increase in ambient pressure because this experiment keeps air-fuel mass ratio to be a constant so that at high ambient pressure, airflow velocity definitely will be smaller due to the increase of air density, and the airflow has less ability to scatter liquid sheets into droplets. Leong et al. [20] found that the increase in ambient pressure leads to the decrease of spray penetration depth when pressure drop and fuel flow rate are held constant. Zheng et al. [42] used

PDPA to measure droplet size distributions and droplet velocity of a prefilming airblast atomizer at different ambient pressures. The results showed that the effect of ambient pressure on the average size and velocity profiles of spray droplets is quite small. This is mainly attributed to the fact that for the specially-designed contraswirling airblast atomizers employed in their study, the atomization mechanism is independent of pressure [42]. Although some of recent studies have focused on the effects of ambient pressure on atomization process of airblast atomizers, the quantitative measurement of the velocity of spray droplets and airstreams in the flow fields with different ambient pressure has not been conducted yet, and influence of ambient pressure on the velocity of spray droplet is unknown.

Moreover, the underlying physics of spray droplets performance at high ambient pressure is unknown. The real operating pressure of airblast atomizers in the combustion chamber has to be several times to the atmospheric pressure so that it turns out to be meaningful to explore the effects of ambient pressure on the spray droplets and the mechanism of the interaction between spray droplets and airstreams at high ambient pressure. The present study presents the effects of ambient pressure, pressure drop ratio and liquid flow rate on the velocity fields of spray droplets and airstreams, and explores the interaction between spray droplets and airstreams at different ambient pressure by quantifying the three-dimensional velocity fields using stereo particle image velocimetry (SPIV) technique. Chapter 1 summarizes the introduction and background of the current study. Chapter 2 presents the experimental setup of high-pressure spray test facility and the data acquisition system on it to record the pressure, temperature and liquid flow rate data. Then, the setup of SPIV and a brief introduction of its mechanism are also presented. Chapter 3 shows the experimental results of SPIV measurements for spray droplets and airstreams with different experimental conditions, i.e. pressure drop ratio, ambient pressure and liquid flow rate and

discusses the interaction between spray droplets and airstreams at different ambient pressures by quantifying the tracing capacity of droplets. Chapter 4 gives a summary of the results and conclusions of the present study.

CHAPTER 2. RESEARCH METHODOLOGY

The current investigation involved the characterizing and measuring the three-dimensional velocity of spray droplets and airstreams in spray flows with different experimental conditions such as ambient pressure, pressure drop ratio and liquid flow rate. The three-dimensional velocity of droplets and airstreams were measured by the SPIV technique which has been widely used to measure the instantaneous velocity fields of in fluids [44–47].

High-pressure Spray Test Facility

The present study was carried out in a specially-designed high-pressure spray test facility where inner pressure is adjustable to meet different experiment requirements. The high-pressure test facility was built in Department of Aerospace Engineering of Iowa State University, and the build of this facility was cooperated with Collins Aerospace. As shown in Fig. 2-1, the chamber is featured by a cylinder body of which diameter is 220 mm and length is 470 mm. There are three spinning windows evenly distributed on the chamber wall at the same level to remove condensed or splashing liquids on the window and to provide a clear view for the SPIV measurement. Three spinning windows, which are independently controlled by three rotor systems, can tolerate 250 psi (1.72 MPa) pressure in maximum. A spinning window has two parts that the inner part can spin very fast to keep clear view, and the outer part is stationary to provide a proper working condition and protection for the inner part. The space between the inner part and the outer part was connected to the inlet of air to offset the pressure difference between the atmospheric pressure and the chamber pressure so that inner part can spin very fast with a small friction force. The chamber was connected to three high-pressure tanks where the total volume is 8 m³, and the maximum feasible pressure is 150psi at full capacity. Several honeycombs were placed in the inlet of the chamber to provide uniform incoming flow as well as reduce turbulence intensity which might affect the

performance of the airblast atomizer. The pressure difference between the inlet pressure of air and the air pressure inside the chamber can be adjusted by a ball valve near the outlet of the high-pressure test facility. The pressure for the liquid injection was independently controlled by a pneumatic valve to provide an accurate liquid flow rate. Liquids and compressed air went into the atomizer from different paths, then mix in the atomizer. A smoke fluid container was connected to the air path to provide tracer particles for SPIV measurement; the average size of tracer particles is $1\ \mu\text{m}$ [48,49].

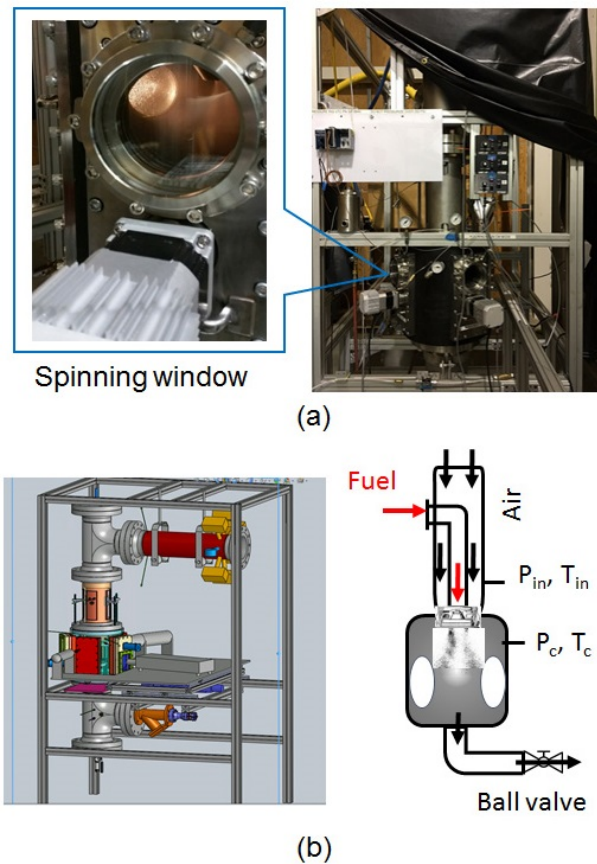


Figure 2-1. (a). A photograph of the high-pressure test facility and one of the specially-designed rotating window; (b). Schematic of the high-pressure test facility.

The airblast atomizer implemented at the center of the chamber was developed by Collins Aerospace as part of the combustor design for NASA's Environmentally Responsible Aviation program to reduce the emission of the greenhouse gas and to meet operability requirements of aircraft engines [50]. The structure of the airblast atomizer is schematically shown in Fig. 2-2. The airblast atomizer consists of an outer air path as the main air path, an inner air path which can inject high-swirling airflow, and a swirling fuel injector between the inner and outer air paths. Most of air ($\approx 93\%$) go through the outer path to provide high shear stress and momentum to scatter liquid sheets/ligaments into spray droplets. Additionally, the percent of air that flows through the inner channel is relatively higher than traditional airblast atomizers to promote rapid mixing of air and liquids [50]. Atomization of liquids happens in the airblast atomizer so only liquid droplets are observed in the flow field rather than liquid sheets/ligaments, which provides convenience for SPIV measurement since droplets could be used as tracer particles to reveal the real flow field of the liquid phase. The diameter of the airblast atomizer is 25.4 mm (1 inch). Pure water was used in this study to meet the safety guideline of the laboratory.

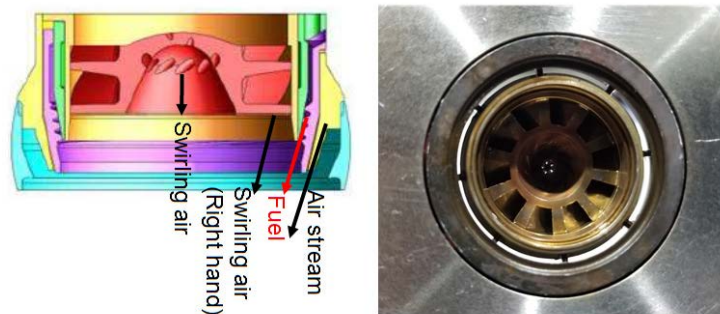


Figure 2-2. *Structure of the airblast atomizer investigated in the present study.*

The schematic diagram of the data acquisition system is shown in Fig. 2-3. The pressure at airflow inlet and inside the chamber were monitored by two pressure transducers (Omega 150psi).

Temperature at the inlet and inside the chamber were also monitored by two K-type thermocouples respectively. The data of pressure transducers and thermocouples were acquired by a DAQ device (National Instruments, 6009) and an acquisition unit (National Instruments cDAQ-9174), respectively. A high-accuracy flowmeter (Omega, FLR1000) was used to monitor the liquid flow rate. A homemade Matlab code collected all these data at a frequency of 10Hz and stored data into a host computer. Fig. 2-4 shows the variation of pressure and temperature with an inlet pressure of 110 psi and a pressure drop ratio of 4% at room temperature. It should be noted that pressure and temperature almost keep constants during the experiment, as a result, spray flow should have a consistent performance during the experiment.

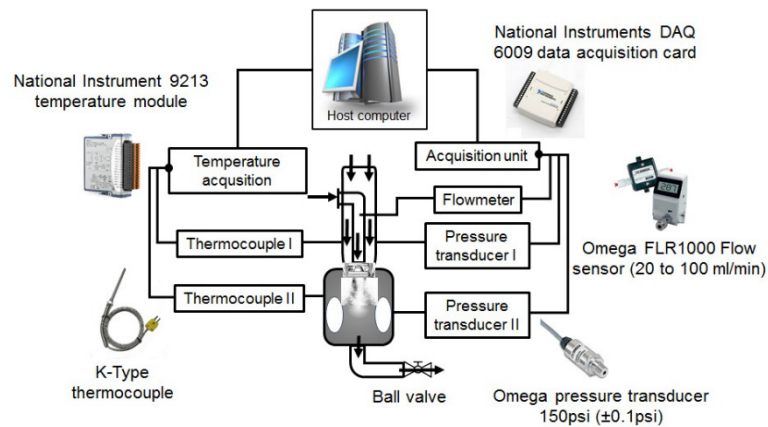


Figure 2-3. The schematic diagram of data acquisition units.

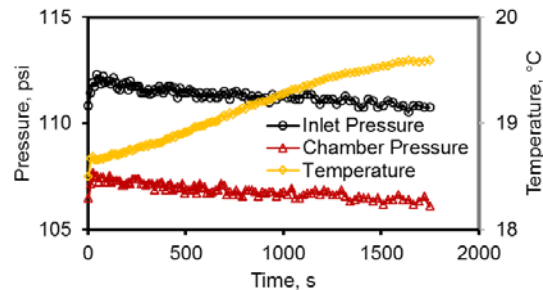


Figure 2-4. A typical acquired data of pressure and temperature during the experiment.

Stereo Particle Image Velocimetry

SPIV is a nonintrusive flow velocity measurement technology, which is widely used for conducting three-dimensional velocity field measurement of fluids [51–54]. SPIV can obtain simultaneous two-dimensional or three-dimensional velocity vector fields by analyzing the displacements of visible tracer particles; these particles are illuminated by a thin double-pulsed laser sheet and recorded by two CCD cameras. The traditional PIV technique was firstly developed in the 1980s by several research groups independently due to the rapid development of high-speed cameras, laser techniques and computer science technologies [55–57]. Generally, PIV technique indicates two-dimensional PIV which could measure two velocity components in a plane. In 2D PIV, the particle-seeded flow field is illuminated by a double-pulsed laser sheet, and then is recorded by a high-speed camera which is perpendicular to the laser plane. Then, the target area is divided into lots of sub-sections which is usually called interrogation areas. The cross-correlation is then conducted among interrogation areas to identify the common particle displacements by detecting the peak value of cross-correlation coefficients as well as the velocity vectors derived from the pixel displacements. The cross-correlation between two interrogation areas is given by Eq. (2.1) where r is the cross-correlation coefficient ranging from -1 to 1 (i.e., 0 indicates no correlation, and 1 and -1 represent maximum correlation). I in Eq. (2.1) is image intensity where superscript a and b indicate the properties of two different images for an image pair of PIV measurement, and subscript m and n are the indexes of interrogation windows.

$$r = \frac{\sum_m \sum_n (I_{mn}^a - \bar{I}^a)(I_{mn}^b - \bar{I}^b)}{\sqrt{(\sum_m \sum_n (I_{mn}^a - \bar{I}^a)^2)(\sum_m \sum_n (I_{mn}^b - \bar{I}^b)^2)}} \quad (2.1)$$

The interrogation window size is normally the power of 2 (e.g., 8, 16, 32) to reduce the computer processing time. Inside the interrogation window, a searching window is set to identify cross-correlation coefficient, and the size of the searching window is determined by the ‘quarter

rule' that searching window size should be approximately a quarter of interrogation window size (e.g., 8pixel \times 8pixel searching window for 32pixel \times 32pixel interrogation window) to reduce the measurement error and image processing time [58]. The time interval between two adjacent laser pulses is determined by allowing particles or droplets to move 8 pixels on average. The interrogation windows often have a 50% overlap to increase the density of velocity vector and measurement accuracy. Once the displacements are obtained by a cross-correlation algorithm, velocity vector fields can be given by Eq. (2.2) where \mathbf{V} , $\Delta\mathbf{x}$, and Δt are the velocity vector, the particle displacement and the time interval between two laser pulses. As a result, the main task is determining particle displacements.

$$\mathbf{V} = \frac{\Delta\mathbf{x}}{\Delta t} \quad (2.2)$$

If a stereoscopic approach is added into traditional PIV measurement, the instantaneous third velocity component in the laser plane could be obtained [47]. One approach to obtain all three velocity components in the laser plane is adding an additional camera from a different view axis. Two cameras at the different view axis can obtain different projections of the same velocity component, and then, the real three-dimensional velocity vectors can be retrieved from these two different projections of velocity vectors. The fundamental principle of SPIV is the same as human eye-sight which is also a stereo vision. Our two eyes can see the same object from two slightly different views, and comparing these differences. Our brain then is able to decode the underlying information contained by these differences and make a three-dimensional interpretation. If we only use one eye to see a moving object, it can barely see the motion away from us. The schematic diagram in Fig. 2-5(a) graphically shows the principle of SPIV and the function of adding an additional camera. It should be noted that the real displacement vector is projected to camera 1 and camera 2 as vector dx_1 and dx_2 respectively. The length and direction of dx_1 and dx_2 are related to

the tilted angle of cameras and the distance from the camera to the observed particle. The real displacement vector can be retrieved if these parameters can be determined. An example of image pairs of SPIV recorded by two cameras at different view axis is also shown in Fig. 2-5(b). It should be pointed out that view 1 is almost the mirror flip image of view 2 since SPIV measurement requires the same view of interest for two cameras. Although view 1 and view 2 are very similar, there are still some visible differences so that real velocity vectors can be obtained by decoding the difference. Applying the cross-correlation algorithm for two cameras can obtain two displacement vector fields. The reconstruction of the real velocity vector field requires two individual vector fields and also needs some spatial parameters which needs to be determined by the calibration procedure.

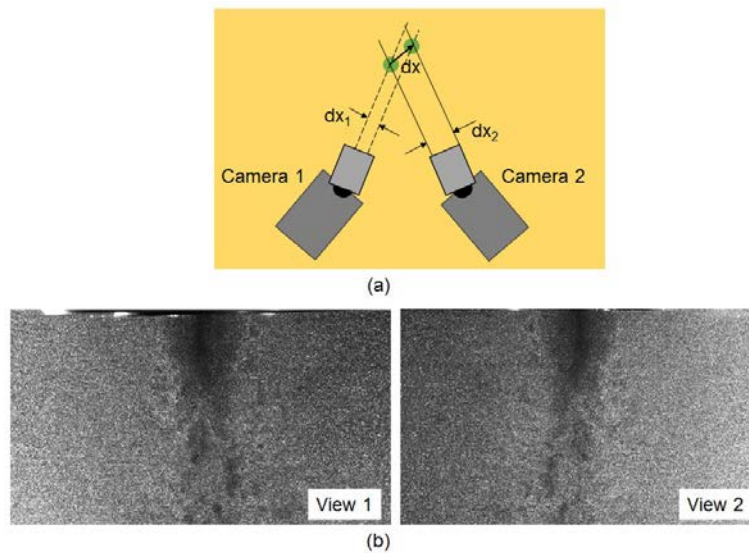


Figure 2-5. (a). *The principle of stereoscopic imaging; (b). An example of two cameras views for SPIV measurement.*

Following the work of Willert [46], a general equation for calculating three true particle displacements (Δx , Δy and Δz) can be given as a function of displacement along the x -axis recorded

by two cameras ($\Delta x_1, \Delta x_2$), displacement along the y -axis ($\Delta y_1, \Delta y_2$) recorded by two cameras and four angles ($\alpha_1, \alpha_2, \beta_1$ and β_2) shown in Fig. 2-6:

$$\begin{cases} \Delta x = \frac{\Delta x_2 \tan \alpha_1 - \Delta x_1 \tan \alpha_2}{\tan \alpha_1 - \tan \alpha_2} \\ \Delta y = \frac{\Delta x_2 \tan \beta_1 - \Delta x_1 \tan \beta_2}{\tan \beta_1 - \tan \beta_2} \\ \Delta z = \frac{\Delta x_2 - \Delta x_1}{\alpha_1 - \alpha_2} \end{cases} \quad (2.3)$$

Angles α_i and β_i (subscript is the index of the camera) are the function of the position of cameras and the true position of particles which is given by:

$$\begin{cases} \tan \alpha_1 = \frac{x_p - x_1}{z_p - z_1} \\ \tan \alpha_2 = \frac{x_p - x_2}{z_p - z_2} \\ \tan \beta_1 = \frac{y_p - y_1}{z_p - z_1} \\ \tan \beta_2 = \frac{y_p - y_2}{z_p - z_2} \end{cases} \quad (2.4)$$

x_p, y_p and z_p are three-dimensional true coordinates of the particle, and x_i, y_i and z_i indicate the true coordinate of the i^{th} camera.

As a result, identifying the real coordinate of cameras and particles is fundamental for the SPIV measurement. Magnification factor of cameras is dependent on the focal length, observation angles, and nominal magnification but measuring all three factors accurately is not easy and complicated for each experiment so a mapping function, which could be linear, second-order or pinhole model, should be obtained before the experiments. The mapping function could be obtained by a careful calibration procedure. Generally, a second-order warping approach is a robust model in most situations [46]. The relationship between true coordinate and image coordinate (i.e. CCD camera coordinate) can be given by:

$$\begin{aligned} x_p &= a_1 x_i^2 + a_2 y_i^2 + a_3 x_i + a_4 y_i + a_5 x_i y_i + a_6 \\ y_p &= b_1 x_i^2 + b_2 y_i^2 + b_3 x_i + b_4 y_i + b_5 x_i y_i + b_6 \end{aligned} \quad (2.5)$$

Twelve unknown variables are easy to be determined using a least-squares algorithm if the coordinate of six objects is already known. The double-faced calibration plate shown in Fig. 2-7 can be used to get this mapping function since there are more than 6 dots on each face which can be used as objects with a known position.

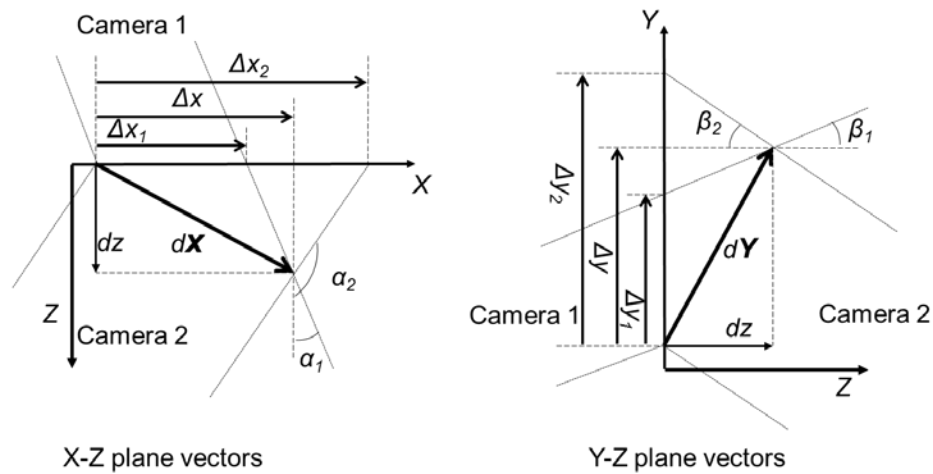


Figure 2-6. Schematic diagram showing the reconstruction of three-dimensional displacement vectors of tracer particles using displacement vectors recorded by two cameras.

Two cameras could be placed at either side of the laser sheet at a favorable viewing angle. The tilt of cameras contributes to the unavoidable distortion of the images. Image distortion or out of focus problem lead to the loss of the out-of-plane velocity component while the in-plane components are also affected by an unrecoverable error due to perspective transformation. The distortion can be corrected by implementing a Scheimpflug optics following the Scheimpflug principle which illustrates that a planar subject that is not parallel to the image plane can be completely in focus by tilting lens until the plane of the camera, the plane of lens and the image plane meet at the same line. The symmetry of two cameras was well studied by Willert [46] who provided a generalized algorithm for the calibration of a nonsymmetrical system.

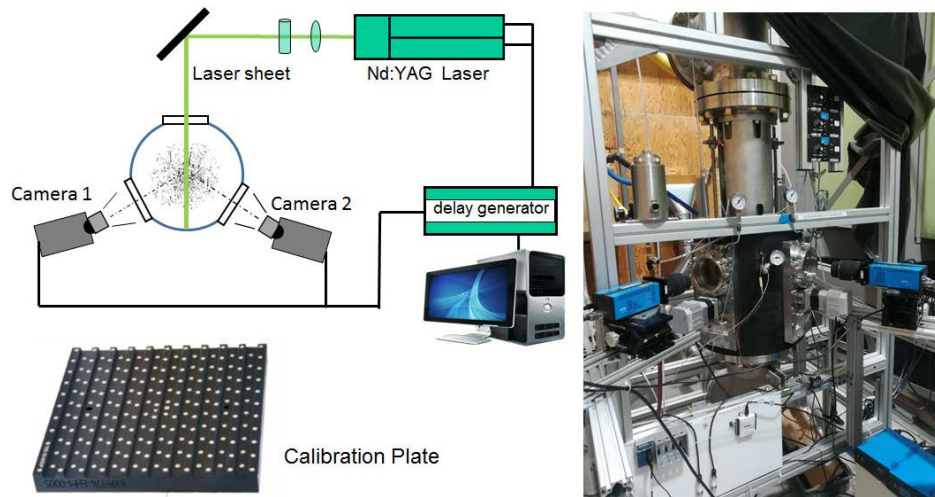


Figure 2-7. Schematic diagram of SPIV setup and the photograph of SPIV setup on the high-pressure test facility at Iowa State University.

The setup of SPIV is shown in Fig. 2-7. Two high-speed cameras (PCO 2000) were arranged at either side of the laser sheet to record the flow field through the transparent rotating windows, and a double-pulsed Nd:YAG laser (EverGreen BigSky 200mJ) was used to shoot a laser sheet through the third rotating window. The laser sheet was aligned along the center of the airblast atomizer. Three windows were evenly distributed on the chamber with an angular angle interval of 120 degrees. Cameras and the laser were synchronized by a delay generator, and raw images were stored into a host computer for image post-processing. The resolution of cameras is 0.026 mm/pixel, and the time interval between two laser pulses ranges from 6 μ s to 8 μ s, which allows particles to have an average displacement of 8 pixels. The calibration procedure and the post-processing for the SPIV were completed by a commercial software supplied by Lavisoin Inc. 500 image pairs were collected for each measurement to obtain time-averaged velocity fields of air and spray droplets [53]. The calibration was done by using a two-level double-sided three-dimensional calibration plate where dot space is defined precisely along the spanwise direction

and in the out-of-plane direction. When the calibration was done in this study, firstly, calibration plate was moved until one side is fully illuminated by the laser sheet and then, the camera focus and Scheimpflug lens was adjusted until the whole plate can be viewed. Secondly, the plate was carefully moved in the direction out the laser sheet to make laser illuminate another side of the calibration plate, and focal length of another camera was adjusted. Finally, a little smoke was exhausted and the focus of two cameras was carefully adjusted to clearly look particles. The calibration procedure is a very essential procedure for SPIV measurement since a bad calibration result could lead to the failure of SPIV measurements.

CHAPTER 3. MEASUREMENT RESULTS AND DISCUSSION

Effects of Pressure Drop Ratio on Spray Characteristics

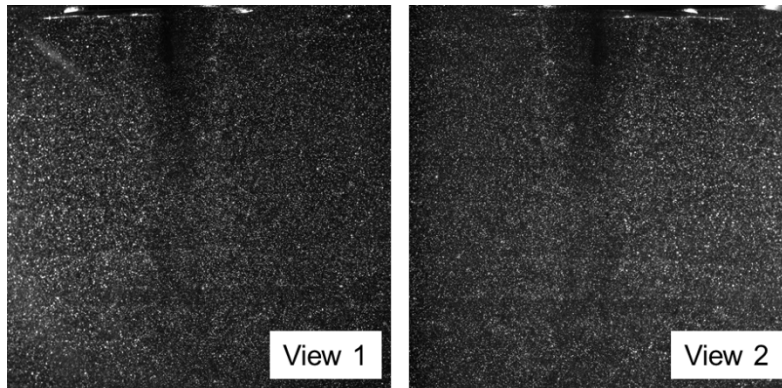


Figure 3-1. *Smoke particle images taken by two different cameras for the SPIV measurement at an ambient pressure of 105 psi and a pressure drop ratio of 2%.*

Airblast atomizers employ the kinetic energy of a flowing airstream to shatter a liquid sheet or a liquid ligament into spray droplets, which needs a large amount of air. The air flow plays an important factor in the atomization process of airblast atomizers, thereby, the characteristics of airstreams were studied by many investigations. It was found that the velocity of airstreams exhausted from airblast atomizers is mainly determined by atomizer geometry, ambient pressure and pressure drop ratio across the airblast atomizer [19]. Pressure drop ratio is defined to be the ratio of pressure drop across the airblast atomizer and the supplied air pressure, which is an important parameter to study atomization since it significantly affects the velocity of the airstream, atomization quality, droplet size and the mixing rate of fuel and air [19]. However, effects of pressure drop ratio on the velocity of spray droplets are rarely discussed by previous investigations [14,23,50]. To reveal the effects of pressure drop ratio on the velocity of spray droplets, both air flow field and liquid flow field should be measured by SPIV technique with different pressure drop ratios. In our study, the smoke tracer particles that is generated by smoke fluids were used

for studying the air flow field; spray droplets were used to measure the velocity field of the liquid. The smoke fluids were stored in a container which is connected to the high-pressure air path, and soon were fully atomized by high-pressure air before exhausted from the atomizer outlet. The average size of smoke particles is usually $1\ \mu\text{m}$ so that it closely follows the motion of air [53].

Fig. 3-1 shows an example of raw images of illuminated smoke particles for SPIV measurements that every particle in the image can be clearly observed. The central area in both views is darker than other parts because the central part has a strong swirling flow where particles have to move outward due to the centrifugal force. The smoke tracer particles used in this experiment have very excellent tracing capacity because of its tiny size (i.e. $\sim 1\ \mu\text{m}$) so that the SPIV measurement can show the motion of airflow by analyzing the trajectories of smoke particles. Pressure drop ratios of 2%, 4% and 6% were used in the present study to investigate the effect of pressure drop ratio on the performance of spray droplets and air since these values of pressure drop ratio are widely used in previous studies [19], and are the real operating condition in aircraft engines.

The velocity vector field of two velocity components in the laser plane and color map for the velocity out of the plane with different pressure drop ratios are shown in Fig. 3-2. It should be noted that the magnitude of all three velocity components increases at a higher pressure drop ratio, which can be observed by the longer vector length in vector maps and darker color in color maps. In this study, the length of vectors increased and the darkness of color maps increased when velocity magnitude rises. The magnitude of velocity was extracted from different locations (i.e. $Y = 12.7\ \text{mm}$, $Y = 25.4\ \text{mm}$ and $Y = 38.1\ \text{mm}$) in color map to provide quantitative comparisons of velocity magnitude at different pressure drop ratio. Extracted velocity profiles are shown in Fig. 3-2 (d-f).

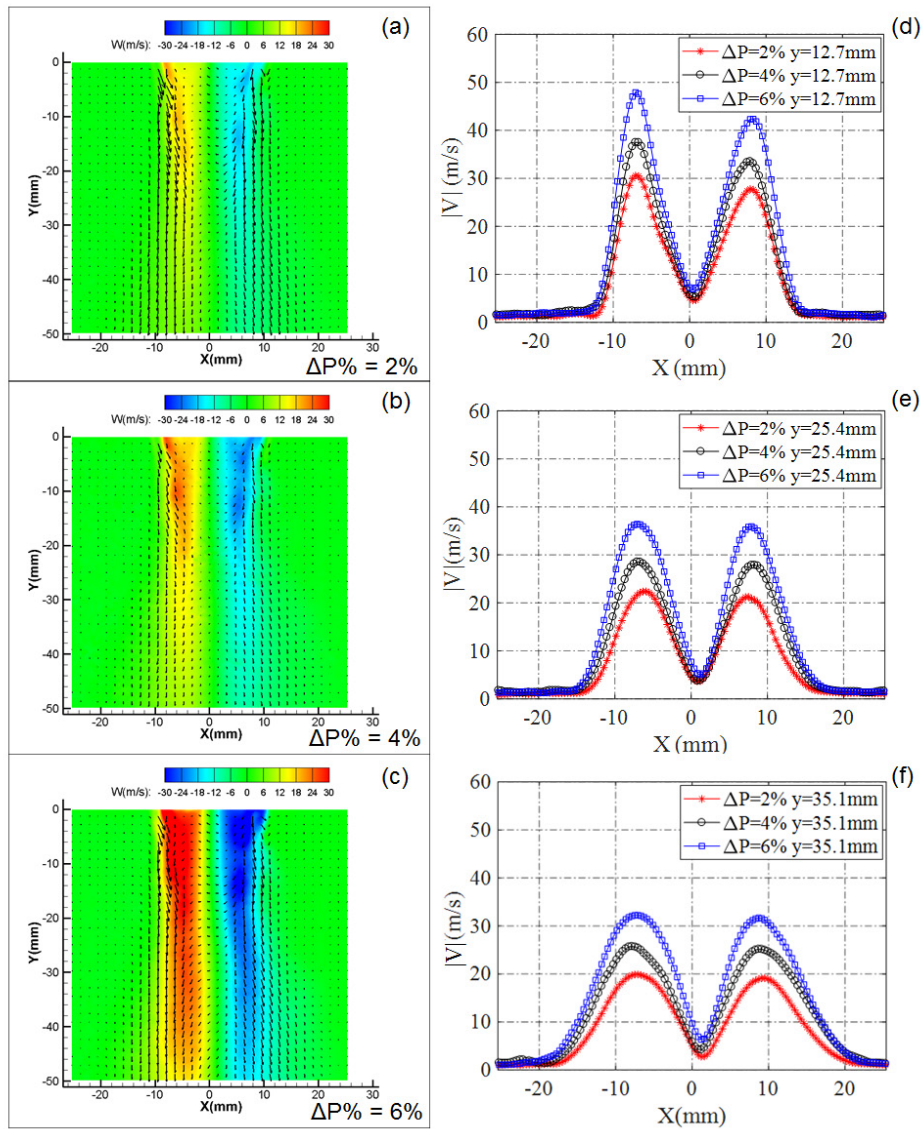


Figure 3-2. Time-averaged velocity vector fields of air at an ambient pressure of 15 psi with different pressure drop ratios: (a) 2%, (b) 4% and (c) 6%. The profile of velocity magnitude of air at three different locations: (d) $Y = 12.7$ mm, (e) $Y = 25.4$ mm and (f) $Y = 35.1$ mm.

Firstly, it was found that the velocity magnitude of air at a high pressure drop ratio is larger than the air at low pressure ratios. The increase of pressure drop ratio provides more energy for the injecting airflow so the average velocity magnitude of high pressure drop ratio is higher.

Atomizer geometry determines the shape of velocity profiles. Primary airflow comes out from the outer path so the velocity away from the center is relatively higher, while the secondary airflow injected from the central part has a low flow rate leading to a low velocity around the atomizer center. Besides, airflows move radially outward as they are moving to the further downstream because the shape of airflows is expanding shown in Fig. 3-2 (a-c). The measurements show that the atomizer could achieve a significantly higher airflow velocity for all three components with a slight increase in pressure drop ratio. Liquid sheets/ligaments are easier to be shattered into droplets with higher shear stress due to faster velocity of air. For a Newtonian fluid, the shear stress is proportional to the velocity gradient given by:

$$\tau = \mu \frac{dV}{dy} \quad (3.1)$$

τ is the shear stress, V is the velocity magnitude, μ is a constant only related to the fluid media for Newtonian fluid like air in this study. Velocity profiles shown in Fig. 3-2 demonstrate that the velocity gradient under higher pressure drop ratio has a larger value since the slope of it is steeper than other cases which have a low-pressure drop ratio.

Turbulence kinetic energy (TKE) is a parameter for evaluating the kinetic energy associated with eddies and turbulence in a flow, which is given by:

$$\text{TKE} = \frac{1}{2} (\overline{(u')^2} + \overline{(v')^2} + \overline{(w')^2}) \quad (3.2)$$

u' , v' and w' are the velocity fluctuation of three components of simultaneous velocity. A higher TKE value indicates the flow is more turbulent which might lead to strong shear stress. It is worthwhile to mention that TKE value is relatively low for the experiment of a 2% pressure drop ratio (Fig. 3-3 (a)) compared with other cases of 4% and 6% (Fig. 3-3 (b, c)). Therefore, the shear stress induced by the velocity fluctuation and turbulent flow is going up with the increase of the pressure drop ratio.

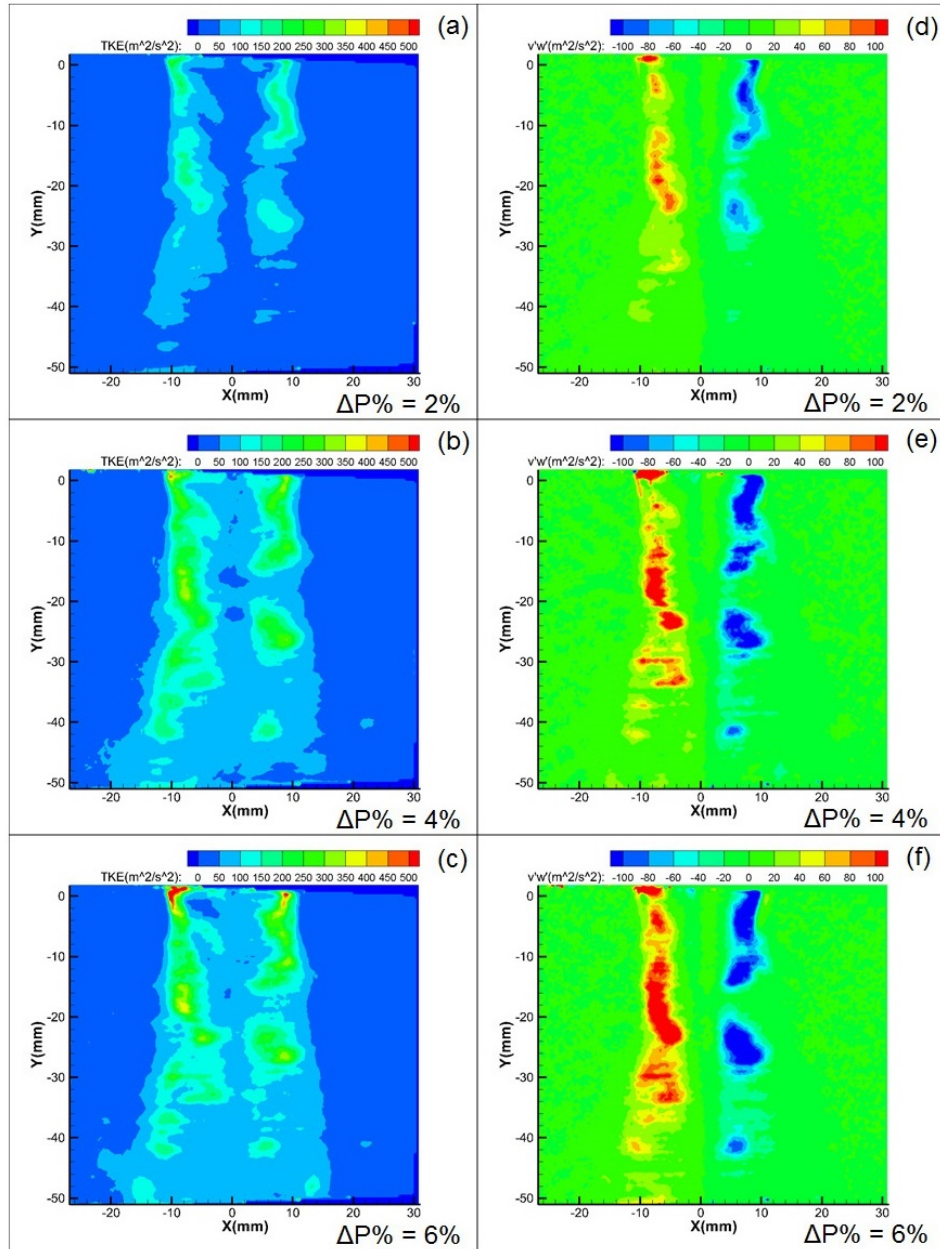


Figure 3-3. *Turbulence kinetic energy and a Reynolds stress component with vertical and azimuthal velocity fluctuation (v' and w') at an ambient pressure of 15 psi with pressure drop ratios: (a) and (f) 2%, (b) and (e) 4%, (c) and (f) 6%.*

The shear stress also should be high when a large pressure drop ratio is selected since the intensity of both velocity fluctuation induced shear stress and mean flow induced shear stress are

stronger. Besides, while the pressure drop ratio is increasing from 4% to 6%, the magnitude of TKE does not have a notable change. This phenomenon indicates that the growth of turbulence intensity is not a linear function of pressure drop ratio. When the increase of pressure drop ratio does not affect TKE, the increase of shear stress only can come from the increment of velocity gradient based on Eq. (3.1). Generally, TKE at the central part is notably lower no matter what the experiment condition is due to the low flow rate of air at the central air path. As air moves to the downstream, TKE gradually goes down because the velocity of air is slower. Reynolds stress is the component of the total stress tensor in a fluid to account for turbulent fluctuations in fluid momentum, which is expressed as:

$$\tau_R = [\overline{u'v'} \quad \overline{u'w'} \quad \overline{v'w'}] \quad (3.3)$$

Fig. 3-3 (d-f) shows the distribution of one Reynolds stress tensor component which has vertical and azimuthal velocity fluctuation terms. Evolution of Reynolds stress is in good consistent with the change of TKE. As pressure drop ratio is increasing, Reynolds stress is becoming stronger but the relationship between them is not linear. The central part of the atomizer also has a very low Reynolds stress value and at the marginal area of the atomizer, the Reynolds stress is very strong. The positive values and negative values of Reynolds stress is influenced by the velocity direction.

It must be mentioned that although one pressure drop ratio corresponds to a specific flow condition, the velocity profiles shown in Fig. 3-2 suggest a potential similarity for all experimental results through a proper normalization method since the position of peaks and valleys over profiles matches very well. Therefore, the pressure drop ratio is probably associated with injection velocity by a relationship. To find this potential similarity, the whole system is simplified to be an isentropic system where the thermodynamic process is both adiabatic and reversible, and in another word,

the system is frictionless without any heat transfer or matter transfer with the external system. The isentropic relationship should start from the definition of enthalpy given by

$$dh = TdS + v dP \quad (3.4)$$

h , T , S , v and P are enthalpy, temperature, entropy and specific volume, respectively. For a perfect gas, $h=C_p T$ where C_p is the specific heat at constant pressure, and substitute the equation of state $PV=RT$ into Eq. (3.4) which is rearranged to obtain the function of dS

$$dS = \frac{C_p}{T} dT - \frac{R}{P} dP \quad (3.5)$$

R is the specific gas constant which for air at standard condition ($T = 273.15$ K, 1 atm), $R=287$ J/(kg·K). Working with Eq. (3.5), an integral is conducted between initial state (subscript 1) and final state (subscript 2), becomes

$$S_2 - S_1 = C_p \ln \left(\frac{T_2}{T_1} \right) - R \ln \left(\frac{P_2}{P_1} \right) \quad (3.6)$$

If the isentropic condition is satisfied, then, $S_2 = S_1$, and C_p is a function of R for the perfect gas, $C_p=\gamma R/(\gamma-1)$ where γ is a constant for air. Substituting this equation into Eq. (3.6), we obtain

$$P_2/P_1 = \left(T_2/T_1 \right)^{\frac{\gamma}{\gamma-1}} \quad (3.7)$$

The pressure ratio is associated with a temperature ratio by Eq. (3.7). Actually, the temperature ratio could govern the Mach number in the system based on the energy equation. The general energy equation can be written as

$$\rho \left[D \left(e + \frac{v^2}{2} \right) / Dt \right] = \rho \dot{q} - \nabla \cdot (P\mathbf{V}) + \rho (\mathbf{f} \cdot \mathbf{V}) \quad (3.8)$$

e , \mathbf{V} , \dot{q} , and \mathbf{f} are internal energy, velocity vector, heat flux, and body force vector, respectively.

The first term at the right side of Eq. (3.8) is zero since the system is adiabatic which heat transfer does not exist at all. The body force term, $\rho(\mathbf{f} \cdot \mathbf{V})$, is also assumed to be negligible. It should be

noted that both variables P and V in the second term are functions of spatial coordinates so it should be written as two separate terms. Eq. (3.8) becomes

$$\rho \left[D \left(e + \frac{V^2}{2} \right) / Dt \right] + \nabla P \cdot \mathbf{V} + P(\nabla \cdot \mathbf{V}) = 0 \quad (3.9)$$

A special equation can be derived from the continuity equation

$$\frac{D\rho}{Dt} + \rho(\nabla \cdot \mathbf{V}) = 0 \quad (3.10)$$

$$\rho \frac{D(P/\rho)}{Dt} = \frac{DP}{Dt} - \frac{P}{\rho} \frac{D\rho}{Dt} \quad (3.11)$$

Substituting Eqs. (3.10) and (3.11) into Eq. (3.9) and assuming a steady-state we obtain

$$D(h + (V)^2/2)/Dt = 0 \quad (3.12)$$

The system is assumed to be steady, inviscid and isentropic until now. The sum of enthalpy and kinetic energy is time-invariant which could build an association between initial state (subscript 1) and final state (subscript 2) expressed as

$$h_1 + (V_1)^2/2 = h_2 + (V_2)^2/2 \quad (3.13)$$

For the tested atomizer, injection velocity is much higher than the airflow velocity at inlet so V_1 is negligible. Velocity is determined by local speed of sound, a , which is a function of temperature, $a=(\gamma RT)^{0.5}$, and velocity could be a function of a , $V=M \cdot a$ where M is local Mach number.

Substituting $h=c_p T$ and $V=Ma$ into Eq. (3.13) and rearrange it

$$\frac{T_2}{T_1} = \left(1 + \frac{\gamma-1}{2} M^2 \right)^{-1} \quad (3.14)$$

Substituting Eq. (3.14) into Eq. (3.7), we have

$$P_2/P_1 = \left(1 + (\gamma-1)/2 M^2 \right)^{-\frac{\gamma}{\gamma-1}} \quad (3.15)$$

P_2 could be written as the sum of P_1 and pressure difference ΔP , $P_2=P_1-\Delta P$. The ratio between ΔP and P_1 is already defined as the pressure drop ratio. It should be noted that if $M \ll 1$ was satisfied,

$(1+aM^2)^b \approx 1+abM^2$. Generally, M ranges from 0.1 to 0.3 in this study which could be regarded as $M \ll 1$. Therefore, Eq. (3.15) could be simplified to be

$$\Delta P\% = \frac{\gamma}{2} M^2 \quad (3.16)$$

Substituting $V=M(\gamma RT)^{0.5}$ into Eq. (3.16), we obtain

$$V_c = \sqrt{2\Delta P\%RT} \quad (3.17)$$

A characteristic velocity for an isentropic, inviscid steady system with low Mach number could be determined by Eq. (3.17). Injection velocity is also affected by the atomizer geometry and some unideal conditions. The real airflow velocity might be proportional to the characteristic velocity. Then, the velocity is normalized by the characteristic velocity.

The color maps of normalized velocity at different pressure drop ratios shown in Fig. 3-4 (a-c) do not have visible differences in the whole flow field. Surprisingly, the profiles of normalized velocity collapse onto one curve, which confirms that velocity fields in this study with different pressure drop ratios are similar. Furthermore, the pressure drop ratio dominates the magnitude of velocity of air exhausted from the airblast atomizer but the structure of the flow is similar in the field.

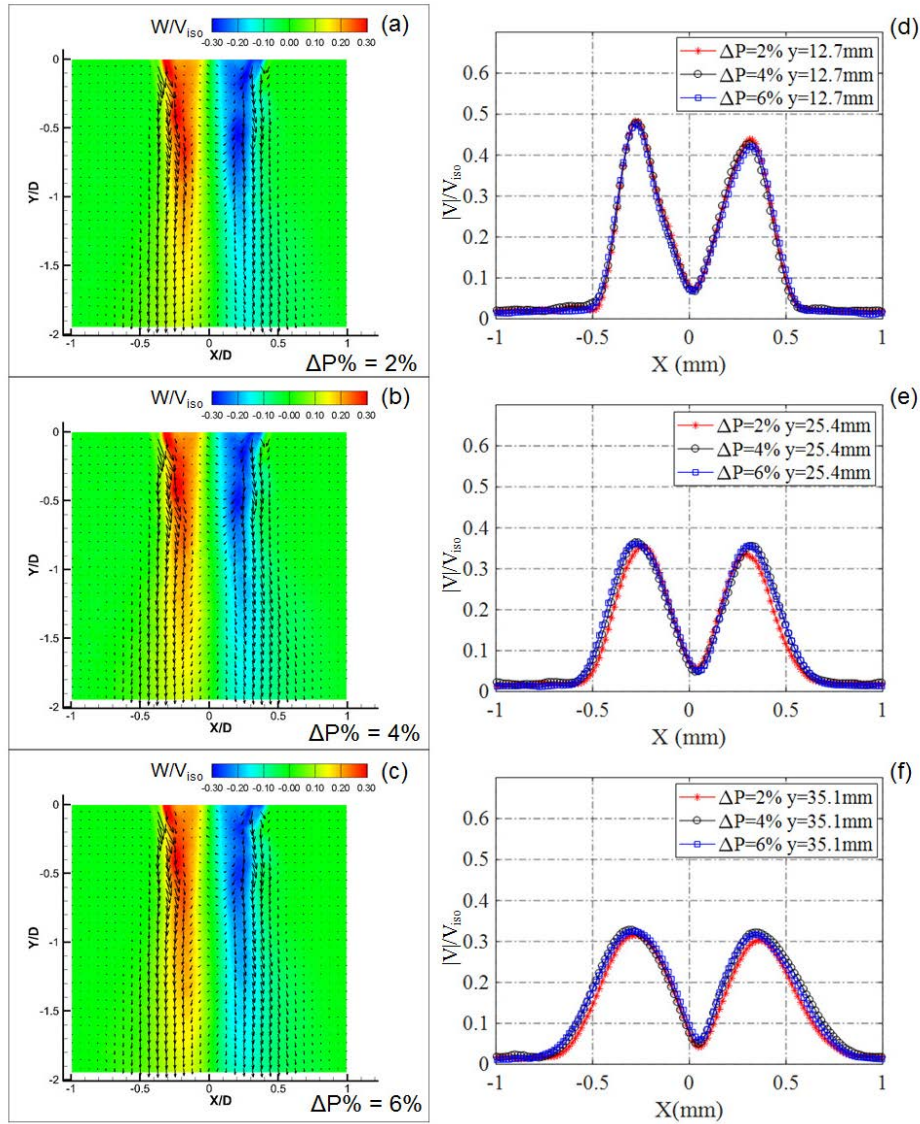


Figure 3-4. Normalized time-averaged velocity fields of air at an ambient pressure of 15 psi with different pressure drop ratios: (a) 2%, (b) 4% and (c) 6%. The profiles of normalized velocity at locations: (d) $Y = 12.7$ mm, (e) $Y = 25.4$ mm and (f) $Y = 35.1$ mm.

Smoke particles could follow the airflow very well but droplets may not closely follow the airflow since the density and size of them are at least one order higher than smoke particles. Moreover, the size of droplets is not as uniform as smoke particles, and it might contribute to a

distinct performance for spray droplets since the tracing capacity of droplets is different. Therefore, investigating the spray flow field is a meaningful and essential work to reveal the interaction between airflow and spray droplets. SPIV measurements are also conducted to study the velocity of spray droplets but smoke particles are substituted by atomized droplets as tracer particles. Light dots in Fig. 3-5, which shows an image pair for SPIV measurements of spray droplets, are droplets illuminated by a laser sheet. Each droplet occupies a $5 \text{ pixel} \times 5 \text{ pixel}$ area in images in average, and droplets distribute evenly in the flow field with a proper density. The tiny size of droplets avoids the double glare points or fringes generated by Mie scattering of droplets [59,60]. As a result, SPIV measurement is possible to be conducted for the spray flow but a multi-pass correlation with window sizes of $32\text{pixel} \times 32\text{pixel}$ and $64\text{pixel} \times 64\text{pixel}$ is operated for SPIV post-processing to avoid losing useful displacement information. 500 image pairs are recorded and then are averaged to obtain time-averaged velocity fields of spray droplets.

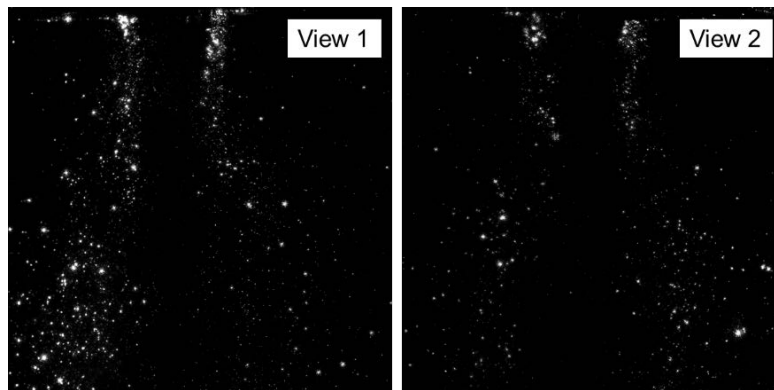


Figure 3-5. A typical image pair of spray droplets for SPIV measurements.

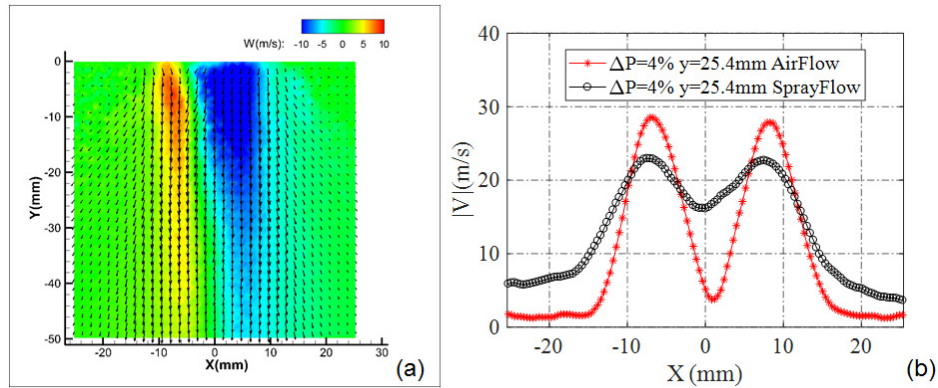


Figure 3-6. (a) The time-averaged velocity vector field and color map of spray droplets at an ambient pressure of 15 psi with a pressure drop ratio of 4%. (b) The velocity profile at $Y = 25.4$ mm of spray droplets and air.

The experimental condition for the spray test is a pressure drop ratio of 4% at atmospheric pressure (15 psi), and a small flow rate of 22.4 ml/min to fully shatter liquid sheets into tiny droplets. The vector field shown in Fig. 3-6 illustrates that spray droplets prefer moving outward in the horizontal direction than the smoke particles, and it also should be noted that the velocity magnitude of spray droplets is much slower than smoke particles at the same experimental conditions. While airflow fields shown in Fig. 3-2 do not have a horizontally outward moving trend especially in the area near the atomizer, droplets could move outward once coming out from atomizer outlet due to a strong centrifugal force provided by a rotating motion. Therefore, it is worthwhile to mention that under atmospheric pressure, airflow does not significantly affect spray flow. The lower velocity of the spray flow also confirms this finding. A velocity profile (Fig. 3-2 (b)) used to compare spray flow and airflow indicates a notable difference between the velocity distributions of spray droplets and air along the spanwise direction. The velocity profile of spray flow (black diamond) is seen to be flatter than the velocity profile of airflow because of the

relatively low peak and bottom values. If there is no airflow in the chamber, under the same ambient pressure, such a low flow rate only provides some large drops (3 mm) with a little azimuthal velocity. For that reason, injected liquids must be shattered into lots of tiny droplets or ligaments by swirling airflow once it comes out from the atomizer but the motion of droplets is not as the same as the airflow since droplets have an initial velocity and high inertia compared with the aerodynamic force exerted over droplets. Some of shattered droplets with high initial velocity move in the central area where airflow velocity is relatively low contributing to the large velocity around the atomizer center of spray flows. Some droplets move radially outward to the area barely affected by the airflow but they are accelerated when they are passing through the outer air path of the tested atomizer. Therefore, droplets in those areas have a relatively high velocity compared to airflows.

The response of spray droplets or any particles can be evaluated by a dimensionless number called Stokes number which is defined as the ratio of the characteristic time of a particle to a characteristic time of the flow or of an obstacle given by

$$Stk = \frac{t_0 V}{l} \quad (3.18)$$

t_0 is characteristic response time. V and l are moving velocity and reference length where particle or droplet diameter is often selected, respectively. In the case of Stokes flow where Reynolds number is much less than unity, the N-S equation could be linearized to be solvable so the theoretical prediction of drag is proportional to the liquid viscosity, velocity and droplet size which is also called Stokes law. The characteristic time of a sphere particle is usually written as [61]

$$t_0 = \frac{\rho_p d_p^2}{18\mu_g} \quad (3.19)$$

ρ_p and d_p are the density and size of particles, and μ_g is the viscosity of surrounding fluids. Substituting Eq. (3.19) into Eq. (3.18), we have

$$\text{Stk} = \frac{\rho_p d_p^2 V}{18 \mu_g l} \quad (3.20)$$

A large Stokes number represents bad tracing accuracy since the response time is too long to allow particles to follow the surrounding flow. Generally, if Stokes number is much less than 1, particles can follow fluid streamlines or fluid motion very closely. Furthermore, for $\text{Stk} < 0.1$, tracing accuracy errors are acceptable. Therefore, a small Stokes number is preferred by SPIV measurements since they need to measure the velocity of flow field by observing tracer particles which should follow the surrounding fluids motion as close as possible. All tests are conducted at room temperature. The average size of smoke particles is approximately 1 μm , and the density of smoke fluids is 1010 kg/m^3 . The reference length, l , is the diameter of the test atomizer (25.4 mm). Therefore, the Stokes number for the smoke particles is 0.04 which is much smaller than unity, and thus, smoke particles can closely follow the airflow to show the real flow field of air. It should be noted that Stokes number is proportional to the particle density and the square of particle size which indicates that spray droplets could have a much larger Stokes number compared with smoke particles since spray droplets have a larger average size ($\sim 20 \mu\text{m}$). The density of spray is determined to be water density but the size could only be approximated due to the limit of the measurement technique. The droplet size could be estimated using raw images for SPIV where resolution is 28.1 $\mu\text{m}/\text{pixel}$; since droplets are very tiny, Mie scattering effect is negligible. Droplet diameter could vary from 56 μm to 280 μm using this method under atmospheric pressure with a pressure drop ratio of 4%. The Stokes number of smoke particles and spray droplets with various diameter shown in Fig. 3-7 illustrates that smoke particles and spray droplets with a diameter less than 5.2 μm could have a good tracing accuracy but spray droplets having an average diameter of

10 μm so most of droplets cannot closely follow the airflow. The size of smoke particles is normally around $1\mu\text{m}$ but the spray droplets can have a much larger diameter at least 20 μm . Therefore, the motion of smoke particles is distinct from spray droplets due to different tracing capacity to the surrounding airflow. Eq. (3.20) shows that Stokes number is more sensitive to the particle size due to the existence of power of two so if droplets could be fully atomized to be very tiny size, the motion of droplets and flow field will be distinct from the current results, and spray flow field may be more likely to airflow velocity field. Other parameters like particle density, velocity, and air viscosity are almost a constant for the tests. In addition, Eq. (3.20) only works for particles in Stokes flow but it already shows that most droplets are not in Stokes flows so Eq. (3.20) needs to be modified to meet the requirement of this study. Finally, Eq. (3.20) does not include the effect of air density but air density plays an important role in acting force over particles. Therefore, more factors should be considered to obtain a new equation to improve Eq. (3.20), and more tests with different ambient should be conducted to confirm it.

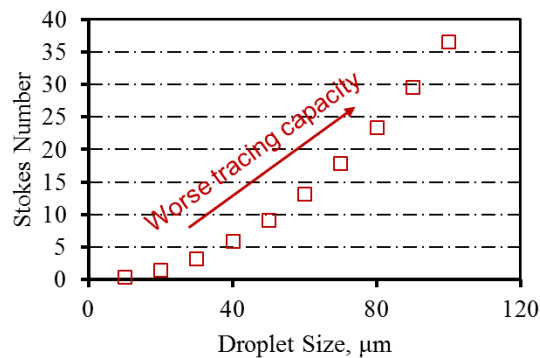


Figure 3-7. Stokes number of droplets with different diameters.

Effects of Ambient Pressure on Spray Characteristics

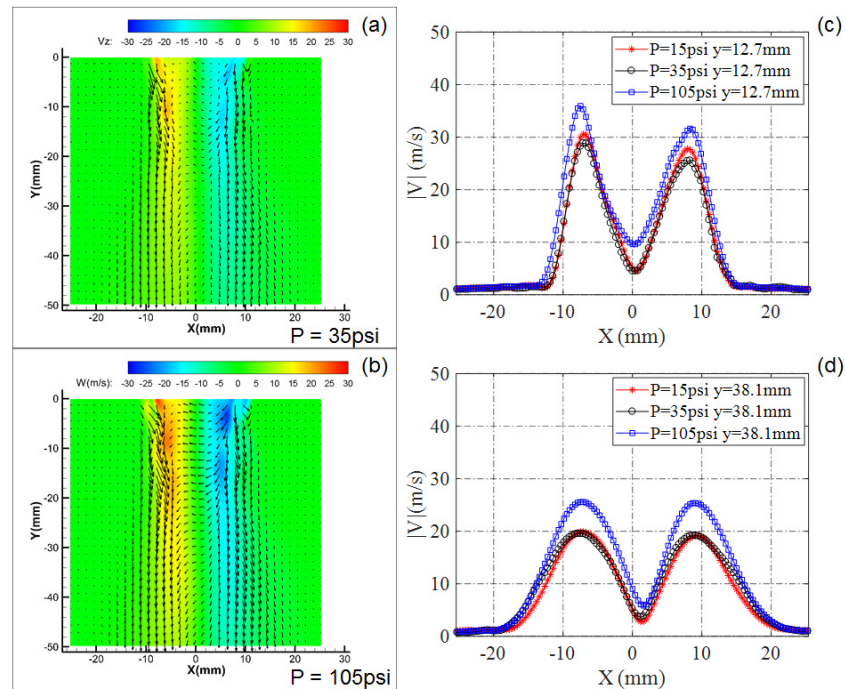


Figure 3-8. Time-averaged airflow velocity fields at a pressure drop ratio of 4% with ambient pressures: (a) 35 psi and (b) 105 psi. The profiles of velocity magnitude at two different locations: (c) $Y = 12.7$ mm and (d) $Y = 38.1$ mm.

Both airflow and spray flow was investigated by SPIV measurement under atmospheric pressure condition but the effects of ambient pressure are still unknown for the flow field of air and spray. In the present study, the airblast atomizer was tested at ambient pressures of 15 psi, 35 psi and 105 psi. The liquid flow rate was kept a constant of 24 ml/min.

Fig. 3-8, 3-9 and 3-10 show the velocity fields measured by SPIV at ambient pressures of 35 psi and 105 psi with pressure drop ratios of 2%, 4%, and 6%, respectively. Velocity fields all look very similar that two main air streams are injected from the outer air path at a high speed with a counter-clockwise swirling flow looking from the top to the bottom injected from the inner air path. Atomizer geometry greatly determines flow patterns so all velocity field is very similar but

flow characteristics like velocity magnitude could be affected by ambient pressure and pressure drop ratio. Ambient pressure is not as important as pressure drop ratio for changing velocity magnitude since at each figure at the same pressure drop ratio but different ambient pressures have a very similar velocity magnitude and velocity vector field which can be seen from similar color distribution. In addition, velocity magnitude is increasing as pressure drop ratio is becoming larger under both low ambient pressure and high ambient pressure.

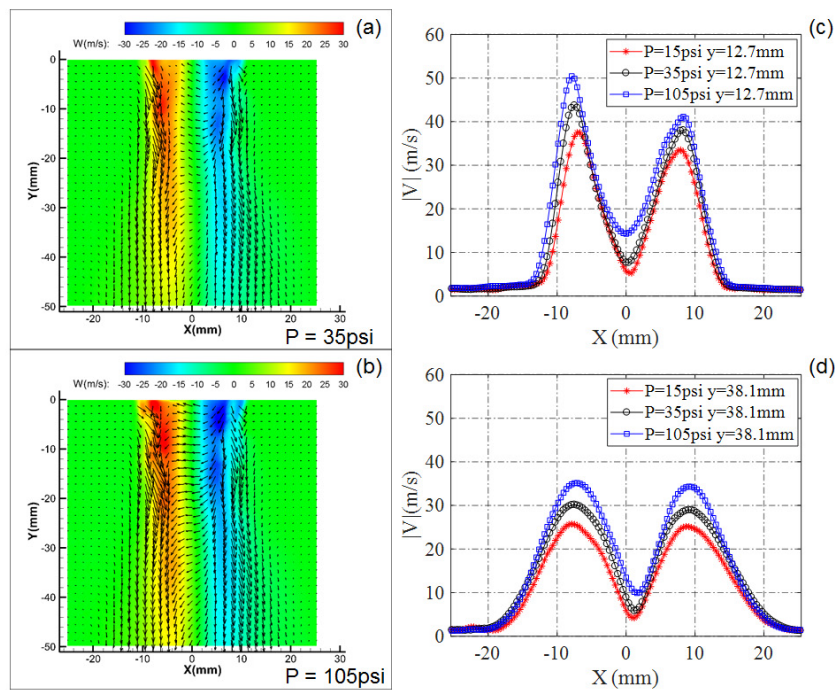


Figure 3-9. Time-averaged air velocity vector fields at a pressure drop ratio of 4% with ambient pressures: (a) 35 psi and (b) 105 psi. The profiles of velocity magnitude at two different locations: (c) $Y = 12.7$ mm and (d) $Y = 38.1$ mm.

This change agrees with the prediction of Eq. (3.17) that injection velocity is a function of pressure drop ratio at a constant temperature. Eq. (3.17) does not include the effect of ambient pressure, and minor differences can be seen from the velocity color map indicating ambient pressure being a secondary factor for injected airflow change. Velocity color map is a useful

qualitative tool to show velocity distribution but a more accurate quantitative method needs to be used to have a more accurate comparison. The velocity profiles at $Y=12.7$ mm and 38.1 mm are extracted from each figure and are shown in each figure. It can be seen that at high ambient pressure (i.e. 105 psi), the velocity magnitude of airflow is notably higher than other cases with low ambient pressure for all pressure drop ratio.

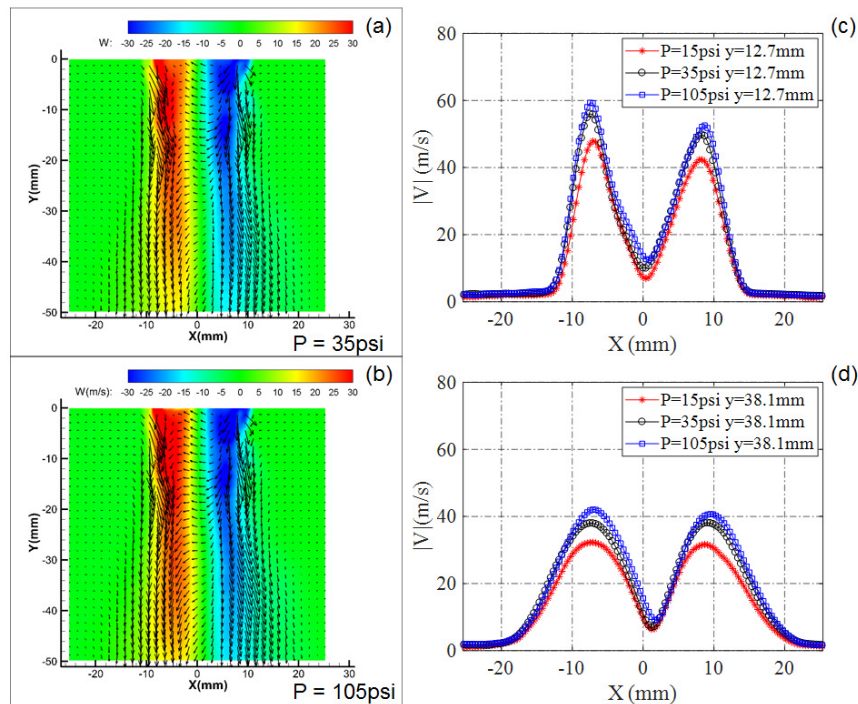


Figure 3-10. Time-averaged air velocity vector fields at a pressure drop ratio of 6% with ambient pressures: (a) 35 psi and (b) 105 psi. The profile of velocity magnitude at two different locations: (c) $Y = 12.7$ mm and (d) $Y = 38.1$ mm.

For example, the blue curve with square symbols in Fig. 3-8 (c) showing the velocity profiles at a pressure drop ratio of 2% and high ambient pressures are higher than other curves representing cases with low ambient pressures. However, Eq. (3.17) and SPIV measurement results show that at the same pressure drop ratio, the characteristic velocity and velocity

distribution in the flow field should be independent of ambient pressure for inviscid, isentropic and steady flows. The analysis is correct to get Eq. (3.17), and the normalized velocity profile can be perfectly matched at a low ambient pressure which also proves the correctness of the theory. Therefore, Eq. (3.17) needs to be improved to include more factors like ambient pressure into consideration, and it will be developed in future. However, it should be noted that ambient pressure plays a secondary factor in spray characteristics compared with the pressure drop ratio.

Ambient pressure is found to greatly affect the characteristics of spray flow at a pressure drop ratio of 4% as shown in Fig. 3-11. Firstly, spray droplets could be accelerated to a higher velocity at a high ambient pressure which is illustrated by comparing the velocity color map and velocity profiles in detail. The color of Fig. 3-11 (b) is stronger than the color in Fig. 3-11 (a), which illustrates that the velocity component of spray droplets in azimuthal direction is larger at a higher ambient pressure. In addition, longer vector length in Fig. 3-11 (b) also indicates the larger velocity of spray droplets under higher ambient pressures. Furthermore, the velocity profiles extracted from $y = 12.7$ mm and $y = 38.1$ mm at different ambient pressure show that velocity magnitude at an ambient pressure of 105 psi is more than twice to the velocity magnitude at an ambient pressure of 15 psi. This is a very interesting phenomenon for spray flow since ambient pressure has a slight effect on the velocity magnitude at the same pressure drop ratio as shown in Fig. 3-9. As a result, spray droplets may also be affected by other factors like the droplet size which is deserved to be studied in detail. Secondly, spray droplets are more likely to move outward under low ambient pressure clearly shown by both the velocity vector field and velocity profiles in figure 3-11. At the high ambient pressure, spray flow velocity could sharply increase from almost zero far away from the atomizer to 50 m/s at the atomizer center as shown in Fig. 3-11 (c) like the velocity profile of airflow but under the same condition, velocity of spray flow gradually increases

from zero to around 20 m/s at the atomizer center. Droplets at high ambient pressure move in a small area near the atomizer but at low ambient pressure, droplets could move far away from the atomizer. This is a very interesting and important phenomenon which indicates in the future, investigating spray characteristics should be always conducted under real working ambient pressure or ambient pressure as high as possible since low ambient pressure does not provide true information about the flow field. If velocity profiles shown in Fig. 3-11 (c) and (d) are compared with velocity profiles in Fig. 3-9 (c) and (d), the evolution of velocity profiles from low ambient pressure to high ambient pressure is likely to be a process of spray flow field gradually approaching airflow field.

To verify this idea, airflow velocity profiles and spray flow velocity profiles at the same experimental conditions are plot together shown in Fig. 3-12. It is very clear that airflow and spray flow has a significant difference under low ambient pressure that spray flow velocity magnitude is notably lower than the airflow but the spray flow affects larger area than the airflow demonstrated by a gradual change of velocity magnitude from the area far away from the atomizer to the area near the atomizer center. While ambient pressure is increasing to 35psi, two velocity profiles are being more similar especially in the downstream area but spray droplets still could move in the radial direction, and the velocity magnitude of spray droplets is still slightly lower. When ambient pressure increase to 105 psi, two velocity profiles almost overlap in the whole field indicating droplets are closely following airflow motion. A little difference between two profiles can be seen in Fig. 3-12 (e) which could be contributed to the asymmetric geometry of secondary swirling air channels which is designed to be axially symmetric.

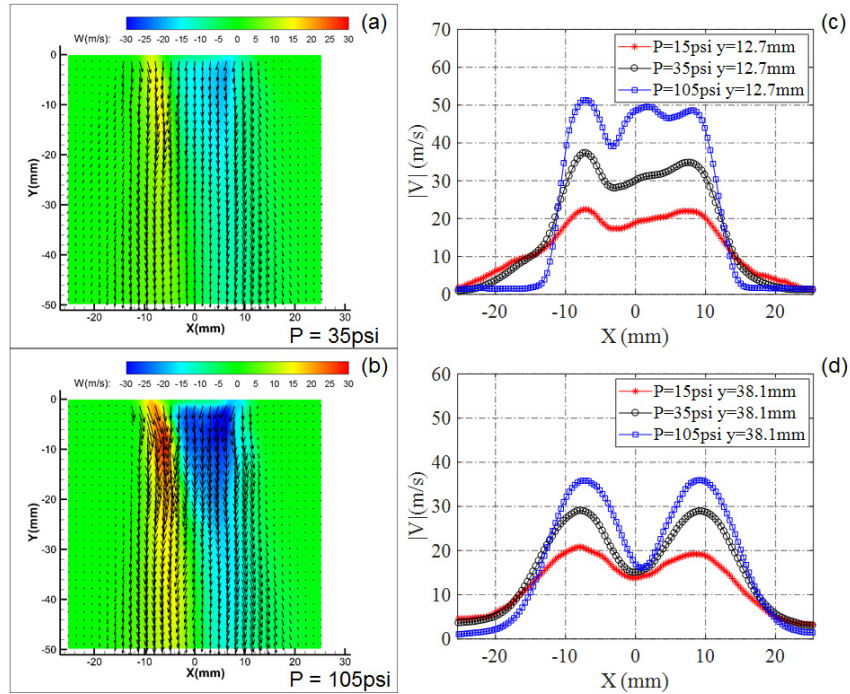


Figure 3-11. Time-averaged velocity vector fields of spray flow at a pressure drop ratio of 4% with ambient pressures: (a) 35 psi and (b) 105 psi. The profiles of velocity magnitude at two different locations: (c) $Y = 12.7$ mm and (d) $Y = 38.1$ mm.

These comparisons demonstrate those spray droplets are more likely to follow the airflow motion at higher ambient pressure. As aforementioned, Stokes number is used to evaluate the tracing capacity of droplets and is given by Eq. (3.20) whereas ambient pressure is not included in that equation. Although there is no pressure term in Eq. (3.20), spray droplets are observed to be much smaller at high ambient pressure so ambient pressure may affect Stokes number of droplets by changing droplet size. The Stokes number is sensitive to the droplet size since it is proportional to the square of droplet diameter. Moreover, air can be denser under high pressure since most of the volume of air is composed of a large amount of empty space between the gas particles, and increasing pressure could easily reduce the amount of empty space.

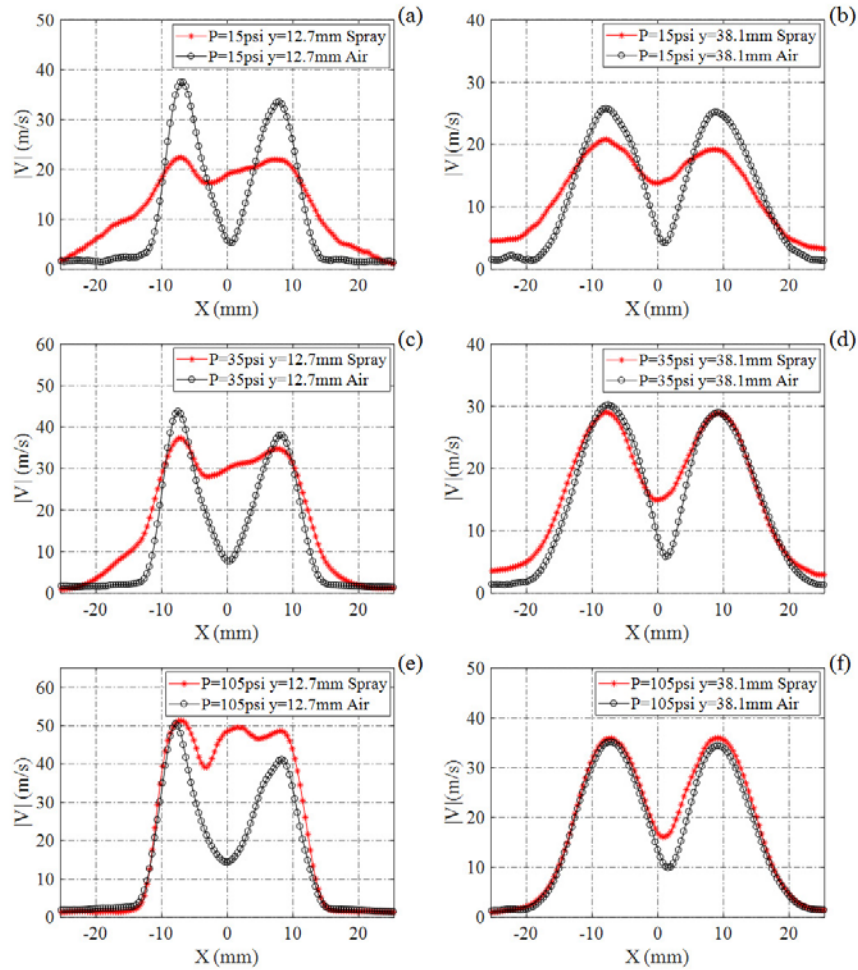


Figure 3-12. Velocity profiles of air and spray droplets at a pressure drop ratio of 4% with ambient pressures: (a, b) 15 psi, (c, d) 35 psi and (e, f) 105 psi at two different locations: $Y = 12.7 \text{ mm}$ and $Y = 38.1 \text{ mm}$.

For an ideal gas, the pressure is proportional to the product of density and temperature given by Eq. (3.21) which is applicable in this study. Temperature is almost a constant during the measurement process so density is only a linear function of pressure indicating under high-pressure condition, air density being much larger than the low pressure. Intuitively, the movement of spray droplets is probably affected by dense air under high ambient pressure since the force exerted by dense air to a droplet is larger than atmospheric air. In this way, therefore, this makes evident that the relaxation time of particle which is defined as the time constant in the exponential decay of the

particle velocity due to drag should include an ambient pressure term. Undoubtedly, the calculation of Stokes number given by Eq. (3.21) should be improved for this purpose.

$$P = \rho RT \quad (3.21)$$

$$D = 6\pi\mu RV \quad (3.22)$$

Eq. (3.21) assumes flow around particles in Stokes flow which is a type of flow that has a Reynolds number much less than one where the drag of sphere particles is given analytically by Eq. (3.22). Air pressure or air density term cannot be found in it since viscosity is a dominant factor for this problem. To estimate the Reynolds number, flow velocity, average droplet diameter, and air density is estimated to be 20m/s, 10 μ m, and 1.23kg/m³, respectively, which are typical values for experiments. In this way, Reynolds number is 20 which is much larger than unity indicating that in this study, flow is not Stokes flow. As a result, a new equation for relaxation time term should be derived for mediate Reynolds number (i.e. Reynolds number less than 500). Deriving relaxation time term is based on the force analysis for a droplet which is assumed to be a sphere due to the existence of surface tension so knowing the drag of a sphere is an important job. Usually, instead of measuring drag force, most of the studies measured drag coefficient, which is a dimensionless number defined by the ratio of drag force and the product of dynamic pressure and a reference, to provide a correlation of physical phenomena to scalable systems. Some well-known and useful theories include Stokes law (Reynolds number < 0.2) given by Eq (3.22), Oseen's correction (Reynolds number < 2) and Newton's viscous drag (Reynolds number > 500). The range of Reynolds number for this study is from about 20 to approximately 500 so none of these models is qualified. Besides, there are also lots of empirical equations to fit the sphere drag coefficient curve which can be perfectly fitted by a complex correlation equation in the whole field

[62]. When Reynolds number is less than 500, an empirical equation found by Schiller and Naumann given by Eq. (3.23) can fit the drag coefficient curve very well [62].

$$C_d = \frac{24}{Re} (1 + 0.15Re^{0.687}) \quad (3.23)$$

Drag could be obtained by it, expressed as

$$D = 3\pi\mu V d_p (1 + 0.15Re^{0.687}) \quad (3.24)$$

Following the procedure of deriving Stokes number for droplets in Stokes flow [61], the equation of motion of droplets is written as

$$\frac{1}{6}\rho_p\pi d_p^3 \frac{dV}{dt} = -3\pi\mu V d_p (1 + 0.15Re^{0.687}) \quad (3.25)$$

Rearrange equation (3.25)

$$\frac{1}{3\pi\mu V d_p (1 + 0.15Re^{0.687})} dV = -\frac{6}{\rho_p\pi d_p^3} dt \quad (3.26)$$

Then, Eq. (3.26) is integrated from initial time (i.e. $t = 0$) and initial velocity (i.e. $V = 0$) to a specific time (t) and velocity (V)

$$t = \frac{\rho_p d^2}{18\mu} \left[\ln\left(\frac{V}{V_0}\right) + 1.46 \ln\left(\frac{1 + 0.15\left(\frac{\rho V d_p}{\mu}\right)^{0.687}}{1 + 0.15\left(\frac{\rho V_0 d_p}{\mu}\right)^{0.687}}\right) \right] \quad (3.27)$$

Generally, velocity is expressed as a function of time but for convenience, Eq. (3.27) shows time being a function of time which could easily obtain the relaxation time. According to the definition of relaxation time [61], velocity should be in the exponential decay of initial velocity, so the relaxation time using Schiller-Naumann equation is given by

$$\tau = \frac{\rho_p d^2}{18\mu} \left[1 + 1.46 \ln\left(\frac{1 + 0.15\left(\frac{\rho V_0 d_p}{\mu e}\right)^{0.687}}{1 + 0.15\left(\frac{\rho V_0 d_p}{\mu}\right)^{0.687}}\right) \right] \quad (3.28)$$

Therefore, a new calculation equation for Stokes number could be written as

$$Stk = \frac{\rho_p V d^2}{18\mu l} \left[1 + 1.46 \ln \left(\frac{1 + 0.15 \left(\frac{\rho d p}{\mu e} \right)^{0.687} V_0^{0.687}}{1 + 0.15 \left(\frac{\rho d p}{\mu} \right)^{0.687} V_0^{0.687}} \right) \right] \quad (3.29)$$

Rearrange Eq. (3.29), we have

$$Stk = \frac{\rho_p V d^2}{18\mu l} \left(1 - 1.46 \ln \left(\frac{1 + 0.15 Re^{0.687}}{1 + 0.15 (Re/e)^{0.687}} \right) \right) \quad (3.30)$$

It was apparent that the term outside the bracket in Eq. (3.30) is the calculation of Stokes number given by Eq. (3.22). The second term in the bracket of Eq. (3.30) is the correction term that includes the effect of air pressure or density on the motion of droplets. If Reynolds number approaches zero, the second term in the bracket approaches zero so that equation (3.30) becomes Eq. (3.20) which used in Stokes flow where Reynolds number is much less than unity. Therefore, Eq. (3.30) could be used for more situations with wider Reynolds number range.

Based on Eq. (3.29), Stokes number for spray droplets at different ambient pressure as a function of average diameter is the plot and compared in Fig. 3-13. The moving velocity of droplets is assumed to be 30 m/s and air viscosity is 1.81×10^{-5} kg·m/s. It was apparent that as ambient pressure is increasing, particles with the same diameter have a higher Stokes number indicating that tracing accuracy is being worse and a droplet is hard to follow air streamlines. Therefore, the airflow velocity field is distinct from the spray flow field at low ambient pressure as shown in Fig. 3-8 since air drag force exerted on spray droplets is not powerful enough to change the motion of droplets or long response time is needed for droplets to change their motion. At atmospheric pressure, Stokes number could easily reach the critical value (i.e. $Stk = 1$) when droplet size increases to 36 μm which is higher than other conditions. Furthermore, although exact droplet size is hard to measure due to the limitation of measurement technique, the effect of ambient pressure on droplet size is apparent seen in Fig. 3-14 that at atmospheric pressure (15 psi), droplets are sparse but each droplet is relatively large but at high ambient pressure (105 psi), droplets are too

small to be seen and their distribution is very dense. Three images shown in Fig. 3-14 have the same liquid flow rate. Fig. 3-13 illustrates that Stokes number is going up when droplet diameter is increasing so large droplets at low pressure have higher Stokes number, and are hard to follow air streamlines but small droplets at high pressure could closely follow airflow since they have low Stokes number and small relaxation time. Moreover, while the particle diameter is larger and larger, the slope of curves is also getting steeper and steeper so Stokes number is growing faster. As a result, low ambient pressure could contribute to relatively large droplet size and small drag force, and both of them will lead to the increase of Stokes number and bad tracing accuracy so the flow field of spray droplets is distinct from airflow velocity field. Therefore, it is easy to understand spray droplet could move radially outward at low ambient pressure but it cannot be observed at high ambient pressure because a velocity component of droplets in azimuthal direction provide a centrifugal force pushing droplets away from the original trajectory at low-pressure situation but droplets motion is greatly affected by airflow which moves outward very slightly at high-pressure situation.

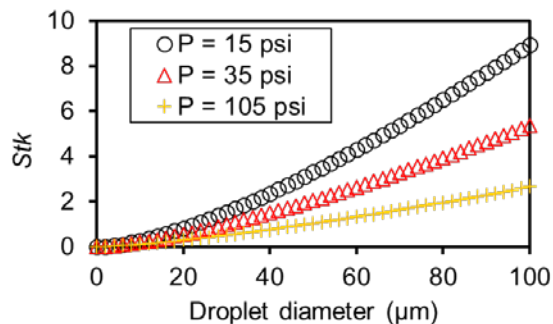


Figure 3-13. *Effects of ambient pressure on tracing capacity of spray droplets at ambient pressure: 15 psi (circle), 35 psi (triangle), and 105 psi (cross).*

Stokes number of droplets with the same diameter is dropping while ambient pressure is decreasing illustrated by Fig. 3-13. When ambient pressure is rising to 35 psi, Stokes number

reaches a unity until droplet diameter reaches 30 μm , and this value for 105 psi ambient pressure is 47 μm . The derivation of Stokes number starts from aerodynamic force analysis where dense air under high-pressure conditions could provide a large force to a droplet. Therefore, the relaxation time for a droplet becomes shorter as pressure is rising or droplets could respond faster in a short time. Undoubtedly, the gradual approach of velocity profiles of spray flow to airflow velocity profiles as ambient pressure is increasing can be contributed to a gradual decrease of Stokes number and improvement of droplets tracing ability. Size effect of atomized droplets is also important that the average droplet size can be observed to get smaller at higher ambient pressure in Fig. 3-14, and small droplets have a small Stokes number and better tracing capacity.

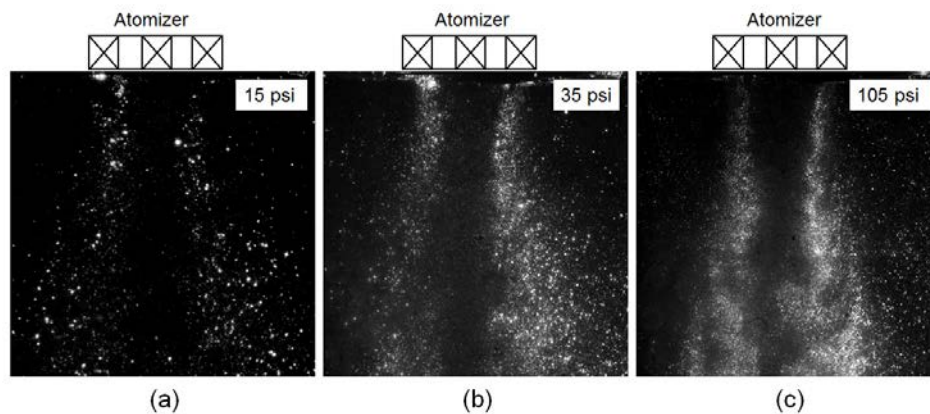


Figure 3-14. *Illuminated spray droplets by a laser sheet with a pressure drop ratio of 4% under different ambient pressures: (a) 15 psi, (b) 35 psi and (c) 105 psi.*

Effects of Liquid Flow Rate on Spray Characteristics

Changing the liquid flow rate for airblast atomizer is demanded frequently to adjust output power for every engine so investigating the effect of liquid flow rate on the atomization process is an important task for real applications of this tested atomizer. Spray characteristics should not have a notable variation when the flow rate is changing in an acceptable range to promise a reliable performance of aircraft engines under different operating condition. The effect of the liquid flow

rate on the performance of the tested airblast atomizer is unknown so investigations are necessary to be conducted. Based on the results of previous sections, fuel injector performance is highly dependent on the ambient pressure and pressure difference. Spray droplets at low ambient pressure do not closely follow airflow streamlines but at high ambient pressure, spray flow can be the same as airflow due to the shrink of average droplet size and increasing air density. It should be noted that Stokes number which shows the tracing accuracy of particles is more sensitive to droplet size since it is proportional to the second power of droplet size. The increase of fuel rate probably changes the average droplet size since there are more liquid injected from the atomizer and the airflow condition is the same while due to the limitation of the measurement technique, the exact average droplet size cannot be measured. To provide some qualitative comparisons, raw images of SPIV showing spray droplets at a pressure drop ratio of 4% with different ambient pressure and liquid flow rate are shown in Fig. 3-15. The maximum flow rate tested in this study is 90 ml/min since this is the maximum liquid flow rate at high ambient pressure condition (105 psi), and to minimize uncertainty, experiments conducted under low and atmospheric pressure also apply for this flow rate number. Droplet size is observed to be notably smaller at high ambient pressure than other low ambient pressure cases. Instead, droplet size does not have a significant change for different liquid flow at any ambient pressures but it was clear that a high flow rate generally gives a higher spatial density for droplets. For the airblast atomizer, air flow rate (from 5×10^5 ml/min to 3.6×10^6 ml/min) is much larger than the liquid flow rate (< 90 ml/min) in volume so airflow is capable to shatter liquid sheets/ligaments no matter what flow rate is provided in this test. Therefore, the average droplet size at the same ambient pressure does not vary a lot. If the droplet size is independent of the liquid flow rate, droplet density must be higher as the liquid flow rate is increasing. Droplet size is observed to be nearly independent of flow rate under all experimental

conditions, which indicates the flow rate may not greatly affect the spray flow since Stokes number does not change a lot.

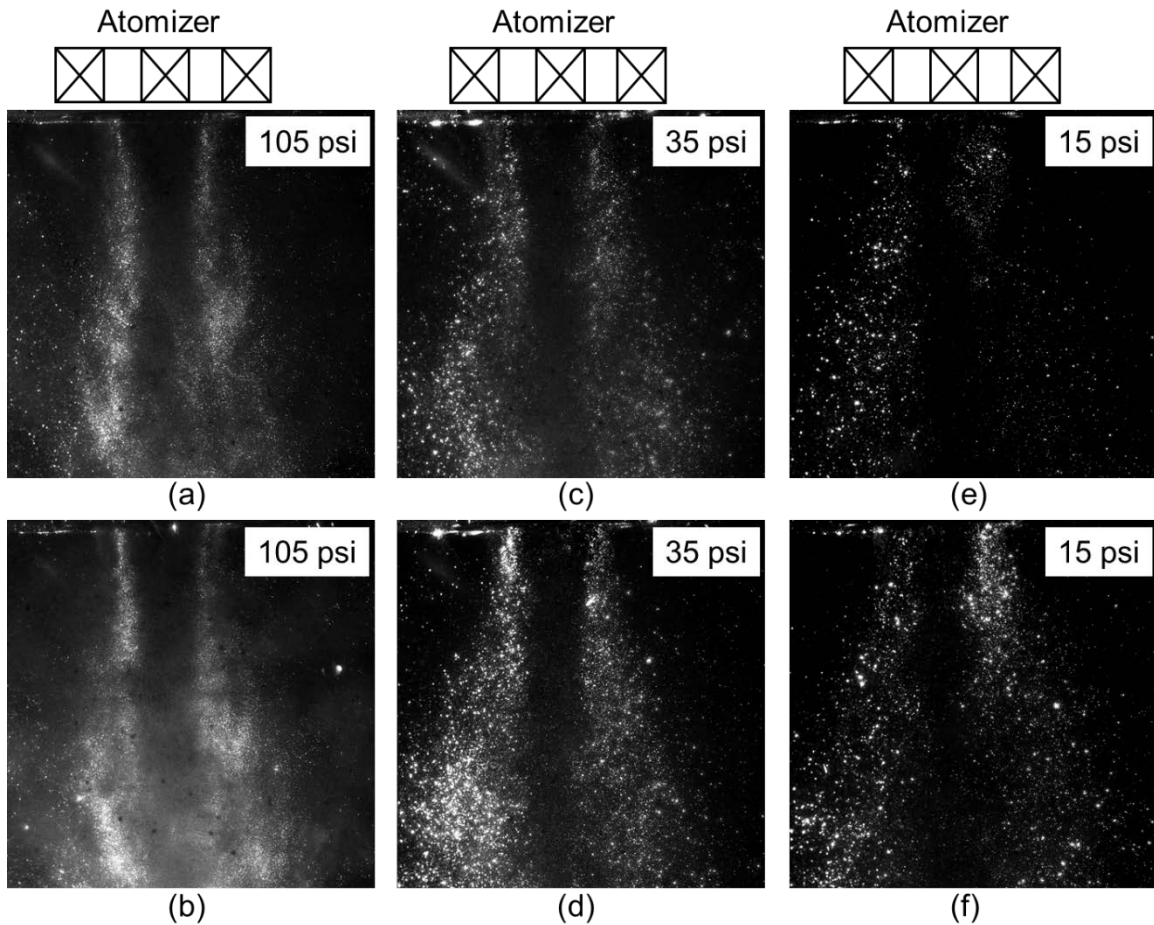


Figure 3-15. *Spray droplets at a pressure drop ratio of 4% with ambient pressures of 105 psi (a, b), 35 psi (c, d) and 15 psi (e, f) and flow rates 24 ml/min (a, c, e) and 90 ml/min (b, d, f).*

Velocity profiles at a pressure drop ratio of 4% with different ambient pressure and different flow are shown in Fig. 3-16, 3-17 and 3-18 where velocity profiles do not show a significant difference which agrees with observations of unchanged droplet size at a different liquid flow rate. Although there are more droplets in the flow field, each of them is driven by the airflow in the same degree since the Stokes number of them is almost the same so the velocity

measured should be the same. With the increase of the number of droplets, the drag of spray flow may have a slight increase because the spray becomes denser for spatial distribution and more droplets are interacting with air. As a result, a slight drop in velocity profile with a large liquid flow rate can be observed. Atomizer performance being independent of flow rate is good to the aircraft engine to have a reliable and consistent performance during the flight time.

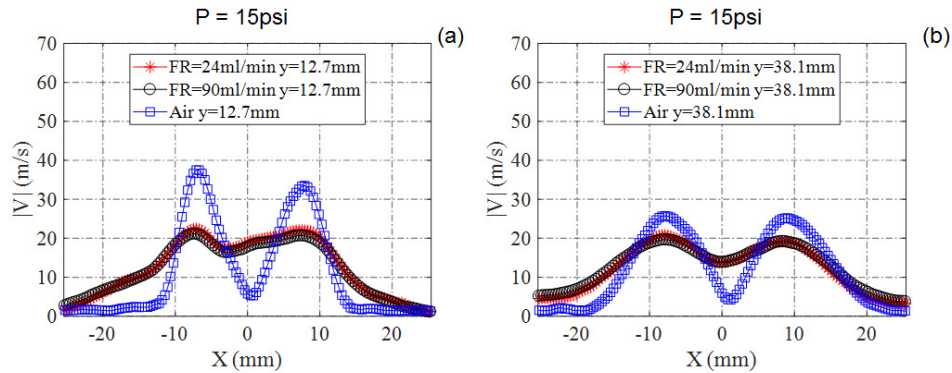


Figure 3-16. Velocity profiles of air and spray flow at a pressure drop ratio of 4% with an ambient pressure 15 psi and flow rates of 24 ml/min and 90 ml/min at two different locations: (a) $Y = 12.7$ mm and (b) $Y = 38.1$ mm.

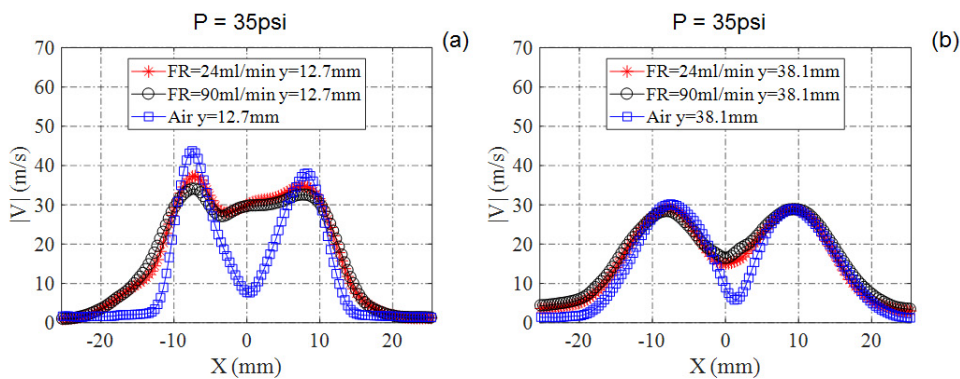


Figure 3-17. Velocity profiles of air and spray flow at a pressure drop ratio of 4% with an ambient pressure 35 psi and flow rates of 24 ml/min and 90 ml/min at two different locations: (a) $Y = 12.7$ mm and (b) $Y = 38.1$ mm.

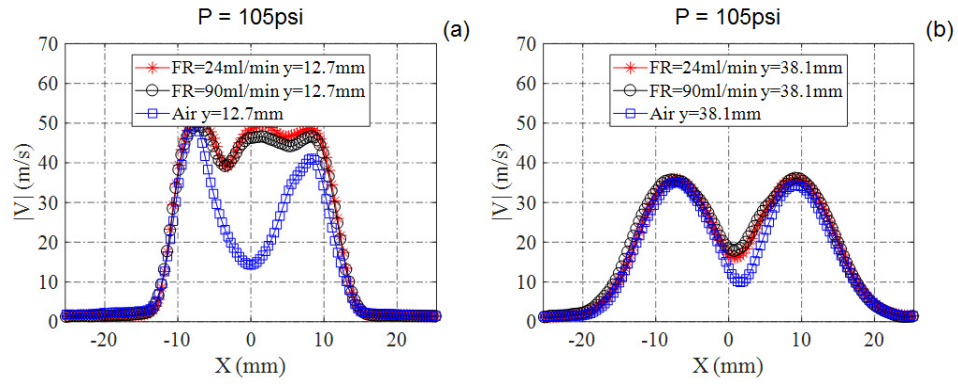


Figure 3-18. Velocity profiles of air and spray flow at a pressure drop ratio of 4% with an ambient pressure 105 psi and flow rates of 24 ml/min and 90 ml/min at two different locations:

(a) $Y = 12.7$ mm and (b) $Y = 38.1$ mm.

CHAPTER 4. CONCLUSION

In the present study, experimental investigations were conducted to evaluate the performance of a swirling airblast atomizer under different working conditions (i.e. ambient pressure, pressure drop ratio and liquid flow rate) using SPIV technique to provide reliable data for the improvement of atomizer design and the verification of flow simulations. A high-pressure spray test facility was built for the present study at Iowa State University, which was collaborated with Collins Aerospace. Using the high-pressure test facility, the effects of pressure drop ratio, ambient pressure and liquid flow rate on the velocity of air and spray droplets are investigated. It was found that the airflow velocity magnitude is greatly affected by pressure drop ratio. An increase of airflow velocity magnitude can be observed when the pressure drop ratio is rising and vice versa. The velocity of air is also slightly influenced by ambient air pressure. At high ambient pressures, velocity magnitude is also observed to have a small increase compared to the velocity magnitude at a lower ambient pressure. A theory based on assumptions of isentropic, steady and inviscid flow is successfully developed to find the relationship between airflow velocity and pressure drop ratio. It should be noted that at atmospheric pressure, airflow velocity should be proportional to the square root of the pressure drop ratio. However, at high ambient pressure conditions, airflow does not satisfy the same rule very well because airflow may not be isentropic when ambient pressure is elevated. Furthermore, ambient pressure also have significant effects on the spray velocity field. While pressure drop ratio is the same, spray droplets will have higher average velocity at high ambient pressure. Moreover, the spray velocity field is much more similar to the airflow velocity field under high ambient pressure conditions (e.g., 105 psi). For instance, while the pressure drop ratio is the same, at atmospheric pressure (i.e. 15 psi), spray flow is observed to have a radially outward motion but most spray droplets do not have velocity in radial

direction under the elevated ambient pressure (105 psi). The influence of ambient pressure on droplets tracing capacity is studied theoretically by analyzing Stokes number of a single droplet. It was found that when ambient air pressure increases, Stokes number becomes significantly smaller, which means droplets are able to closely follow the motion of air. This result suggests that experiments should be conducted under high ambient pressure in future for atomization experiment since spray flow velocity is sensitive to the ambient pressure. Finally, while liquid flow rate changes from 24ml/min to 90ml/min, the change of spray droplets velocity is very slight at all ambient air pressures. It should be noted that the change of liquid flow rate does not have a notable effect on the velocity field of spray droplets for the airblast atomizer so this fuel injector can provide reliable and consistent performance under different flight conditions.

REFERENCES

- [1] L. Durdina, J. Jedelsky, M. Jicha, Investigation and comparison of spray characteristics of pressure-swirl atomizers for a small-sized aircraft turbine engine, *Int. J. Heat Mass Transf.* 78 (2014) 892–900. doi:10.1016/j.ijheatmasstransfer.2014.07.066.
- [2] C. Galbiati, S. Tonini, P. Conti, G.E. Cossali, Numerical simulations of internal flow in an aircraft engine pressure swirl atomizer, *J. Propuls. Power.* 32 (2016) 1433–1441. doi:10.2514/1.B35944.
- [3] D. Sivakumar, S.K. Vankeswaram, R. Sakthikumar, B.N. Raghunandan, J.T.C. Hu, A.K. Sinha, An experimental study on jatropha-derived alternative aviation fuel sprays from simplex swirl atomizer, *Fuel.* 179 (2016) 36–44. doi:10.1016/j.fuel.2016.03.050.
- [4] A.H. Lefebvre, M. Suyari, Film thickness measurements in a simplex swirl atomizer, *J. Propuls. Power.* 2 (1986) 528–533. doi:10.2514/3.22937.
- [5] W. Klaypradit, Y.W. Huang, Fish oil encapsulation with chitosan using ultrasonic atomizer, *LWT - Food Sci. Technol.* 41 (2008) 1133–1139. doi:10.1016/j.lwt.2007.06.014.
- [6] J. Jedelsky, M. Jicha, J. Slama, J. Otahal, Development of an effervescent atomizer for industrial burners, *Energy and Fuels.* 23 (2009) 6121–6130. doi:10.1021/ef900670g.
- [7] G.A. Vijay, N.S.V. Moorthi, A. Manivannan, Internal and external flow characteristics of swirl atomizers: A review, *At. Sprays.* 25 (2015) 153–188. doi:10.1615/AtomizSpr.2014010219.
- [8] E.J. Lee, S.Y. Oh, H.Y. Kim, S.C. James, S.S. Yoon, Measuring air core characteristics of a pressure-swirl atomizer via a transparent acrylic nozzle at various Reynolds numbers, *Exp. Therm. Fluid Sci.* 34 (2010) 1475–1483. doi:10.1016/j.expthermflusci.2010.07.010.
- [9] C. Yoon, S.D. Heister, G. Xia, C.L. Merkle, Numerical modeling of injection of shear-thinning gel propellants through plain-orifice atomizer, *J. Propuls. Power.* 27 (2011) 944–954. doi:10.2514/1.B34135.
- [10] N.K. Rizk, A.H. Lefebvre, Internal Flow Characteristics of Simplex Swirl Atomizers, *J. Propuls. Power.* 1 (1985) 193–199. doi:https://doi.org/10.2514/3.22780.
- [11] Y. Fan, N. Hashimoto, H. Nishida, Y. Ozawa, Spray characterization of an air-assist pressure-swirl atomizer injecting high-viscosity Jatropha oils, *Fuel.* 121 (2014) 271–283. doi:10.1016/j.fuel.2013.12.036.
- [12] R. Feddema, Effect of aviation fuel type and fuel injection conditions on the spray characteristics of pressure swirl and hybrid air blast fuel injectors, Purdue University, 2013. <http://search.proquest.com/docview/1518149493>.

- [13] Larry Kin Bong Li, An experimental study on air-blast atomizer of viscoelastic liquids, University of British Columbia, 2006. doi:10.1016/j.bbapap.2013.06.007.
- [14] A.A. Rizkalla, A.H. Lefebvre, The Influence of Air and Liquid Properties on Airblast Atomization, *J. Fluids Eng.* 97 (1975) 316–320. doi:10.1115/1.3447309.
- [15] A.A. Rizkalla, A.H. Lefebvre, Influence of liquid properties on airblast atomizer spray characteristics, *J. Eng. Gas Turbines Power.* 97 (1975) 173–177. doi:10.1115/1.3445951.
- [16] N.K. Rizk, A.H. Lefebvre, Influence of atomizer design features on mean drop size, *AIAA J.* 21 (1983) 1139–1142. doi:10.2514/3.8217.
- [17] N.K. Rizk, A.H. Lefebvre, The influence of liquid film thickness on airblast atomization, *J. Eng. Gas Turbines Power.* 102 (1980) 706–710. doi:10.1115/1.3230329.
- [18] X.F. Wang, A.H. Lefebvre, Influence of ambient air pressure on pressure-swirl atomizer spray characteristics, in: *Proc. ASME Turbo Expo*, 1987. doi:10.1115/2001-GT-0043.
- [19] A. Jasuja, *Structure of Gas Turbine Fuel Spray*, Cranfield University, 2001.
- [20] M. Leong, V. McDonell, G. Samuelsen, Effect of ambient pressure on an airblast spray injected into a crossflow, *J. Propuls. Power.* (2001).
- [21] M. Chrigui, I. V. Roisman, F.Z. Batarseh, A. Sadiki, C. Tropea, Spray Generated by an Airblast Atomizer Under Elevated Ambient Pressures, *J. Propuls. Power.* 26 (2010) 1170–1183. doi:10.2514/1.47833.
- [22] H.J. Kim, S.H. Park, C.S. Lee, A study on the macroscopic spray behavior and atomization characteristics of biodiesel and dimethyl ether sprays under increased ambient pressure, *Fuel Process. Technol.* 91 (2010) 354–363. doi:10.1016/j.fuproc.2009.11.007.
- [23] K. Rajamanickam, S. Basu, Insights into the dynamics of spray-swirl interactions, *J. Fluid Mech.* 810 (2017) 82–126. doi:10.1017/jfm.2016.710.
- [24] K. Rajamanickam, S. Basu, Insights into the dynamics of conical breakdown modes in coaxial swirling flow field, *J. Fluid Mech.* 853 (2018) 72–110. doi:10.1017/jfm.2018.549.
- [25] K. Rajamanickam, S. Basu, On the dynamics of vortex–droplet interactions, dispersion and breakup in a coaxial swirling flow, *J. Fluid Mech.* 827 (2017) 572–613. doi:10.1017/jfm.2017.495.
- [26] K.P. Shanmugasadas, S.R. Chakravarthy, R.N. Chiranthan, J. Sekar, S. Krishnaswami, Characterization of wall filming and atomization inside a gas-turbine swirl injector, *Exp. Fluids.* 59 (2018) 0. doi:10.1007/s00348-018-2606-0.
- [27] Z. Wu, L. Wang, J.A. Badra, W.L. Roberts, T. Fang, GDI fuel sprays of light naphtha, PRF95 and gasoline using a piezoelectric injector under different ambient pressures, *Fuel.* 223 (2018) 294–311. doi:10.1016/j.fuel.2018.03.009.

- [28] G.E. Lorenzetto, A.H. Lefebvre, Measurements of Drop Size on a Plain-Jet Airblast Atomizer, *AIAA J.* 15 (1977) 1006–1010. doi:10.2514/3.60742.
- [29] N.K. Rizk, A.H. Lefebvre, Spray characteristics of plain-jet airblast atomizers., 106 (1983) 634–638. doi:10.1115/83-gt-138.
- [30] R. Harari, E. Sher, Optimization of a Plain-jet Airblast Atomizer, *At. Sprays.* 7 (1997) 97–113. doi:10.1615/AtomizSpr.v7.i1.50.
- [31] B. Sauer, A. Sadiki, J. Janicka, Numerical analysis of the primary breakup applying the embedded DNS approach to a generic prefilming airblast atomizer, *J. Comput. Multiph. Flows.* 6 (2014) 179–192. doi:10.1260/1757-482X.6.3.179.
- [32] M. Volz, L. Nittel, P. Habisreuther, N. Zarzalis, Numerical Study of Liquid Film Characteristics at Varying Operating Conditions in Prefilmer Airblast Atomizer, *Chemie-Ingenieur-Technik.* 88 (2016) 192–199. doi:10.1002/cite.201500011.
- [33] S. Carmi, M.R. Ghassemzadeh, Viscosity and spray formation studies of coal-oil mixtures, *Fuel.* 60 (1981) 529–533. doi:10.1016/0016-2361(81)90117-4.
- [34] A. Mansour, N. Chigier, Air-blast atomization of non-Newtonian liquids, *J. Nonnewton. Fluid Mech.* 58 (1995) 161–194. doi:10.1016/0377-0257(95)01356-Z.
- [35] I.A. Ibrahim, T.M. Farag, M.E. Abdel-baky, A.K. Abd El-samed, H.M. Gad, Experimental study of spray combustion characteristics of air-blast atomizer, *Energy Reports.* 6 (2020) 209–215. doi:10.1016/j.egy.2019.12.014.
- [36] D. Kim, J.H. Im, H. Koh, Y. Yoon, Effect of ambient gas density on spray characteristics of swirling liquid sheets, *J. Propuls. Power.* 23 (2007) 603–611. doi:10.2514/1.20161.
- [37] R. Ma, B. Dong, Z. Yu, T. Zhang, Y. Wang, W. Li, An experimental study on the spray characteristics of the air-blast atomizer, *Appl. Therm. Eng.* 88 (2015) 149–156. doi:10.1016/j.applthermaleng.2014.11.068.
- [38] H.M. Gad, I.A. Ibrahim, M.E. Abdel-baky, A.K. Abd El-samed, T.M. Farag, Experimental study of diesel fuel atomization performance of air blast atomizer, *Exp. Therm. Fluid Sci.* 99 (2018) 211–218. doi:10.1016/j.expthermflusci.2018.07.006.
- [39] K. Merkle, H. Haessler, H. Büchner, N. Zarzalis, Effect of co- and counter-swirl on the isothermal flow- and mixture-field of an airblast atomizer nozzle, *Int. J. Heat Fluid Flow.* 24 (2003) 529–537. doi:10.1016/S0142-727X(03)00047-X.
- [40] F.Z. Batareseh, M. Gnirß, I. V. Roisman, C. Tropea, Fluctuations of a spray generated by an airblast atomizer, *Exp. Fluids.* 46 (2009) 1081–1091. doi:10.1007/s00348-009-0612-y.
- [41] P.J. Schmid, Application of the dynamic mode decomposition to experimental data, *Exp. Fluids.* 50 (2011) 1123–1130. doi:10.1007/s00348-010-0911-3.

- [42] Q.P. Zheng, A.K. Jasuja, A.H. Lefebvre, Structure of airblast sprays under high ambient pressure conditions, *J. Eng. Gas Turbines Power.* 3 (1996). doi:10.1115/96-GT-131.
- [43] S.K. Chen, A.H. Lefebvre, J. Rollbuhler, Influence of ambient air pressure on effervescent atomization, *J. Propuls. Power.* 9 (1993) 10–15. doi:10.2514/3.11479.
- [44] S. Ghaemi, P. Rahimi, D. Nobes, Evaluation of StereoPIV measurement of droplet velocity in an effervescent spray, *Int. J. Spray Combust. Dyn.* 2 (2010) 103–123. doi:10.1260/1756-8277.2.2.103.
- [45] H. Hu, T. Saga, T. Kobayashi, N. Taniguchi, A study on a lobed jet mixing flow by using stereoscopic particle image velocimetry technique, *Phys. Fluids.* 13 (2001) 3425–3441. doi:10.1063/1.1409537.
- [46] C. Willert, Stereoscopic digital particle image velocimetry for application in wind tunnel flows, *Meas. Sci. Technol.* 8 (1997) 1465–1479. doi:10.1088/0957-0233/8/12/010.
- [47] A.K. Prasad, Stereoscopic particle image velocimetry, *Exp. Fluids.* 29 (2000) 103–116. doi:10.1007/s003480000143.
- [48] L. Gao, Y. Liu, W. Zhou, H. Hu, An experimental study on the aerodynamic performance degradation of a wind turbine blade model induced by ice accretion process, *Renew. Energy.* 133 (2019) 663–675. doi:10.1016/j.renene.2018.10.032.
- [49] R.S. Volkov, P.A. Strizhak, Research of temperature fields and convection velocities in evaporating water droplets using Planar Laser-Induced Fluorescence and Particle Image Velocimetry, *Exp. Therm. Fluid Sci.* 97 (2018) 392–407. doi:10.1016/j.expthermflusci.2018.05.007.
- [50] S.D. Pack, J.A. Ryon, G.A. Zink, D.D. Dvorak, J.L. Goeke, Spray Diagnostics of a Low NO_x Air Blast Atomizer for NASA ERA N + 2 Program, in: 25th Annu. Conf. Liq. At. Spray, Syst. Am., Pittsburgh, 2013.
- [51] H. Hu, T. Saga, T. Kobayashi, N. Taniguchi, Simultaneous measurements of all three components of velocity and vorticity vectors in a lobed jet flow by means of dual-plane stereoscopic particle image velocimetry, *Phys. Fluids.* 14 (2002) 2128–2138. doi:10.1063/1.1481741.
- [52] H. Hu, T. Saga, T. Kobayashi, N. Taniguchi, Mixing process in a lobed jet flow, *AIAA J.* 40 (2002) 1339–1345. doi:10.2514/2.1793.
- [53] W. Zhou, H. Hu, Improvements of film cooling effectiveness by using Barchan dune shaped ramps, *Int. J. Heat Mass Transf.* 103 (2016) 443–456. doi:10.1016/j.ijheatmasstransfer.2016.07.066.
- [54] W. Zhou, H. Hu, A novel sand-dune-inspired design for improved film cooling performance, *Int. J. Heat Mass Transf.* 110 (2017) 908–920. doi:10.1016/j.ijheatmasstransfer.2017.03.091.

- [55] I. Grant, Particle image velocimetry: A review, *Proc. Inst. Mech. Eng. Part C J. Mech. Eng. Sci.* 211 (1997) 55–76. doi:10.1243/0954406971521665.
- [56] C.E. Willert, M. Gharib, Digital particle image velocimetry, *Exp. Fluids.* 10 (1991) 181–193. doi:10.1007/BF00190388.
- [57] J. Westerweel, G.E. Elsinga, R.J. Adrian, Particle Image Velocimetry for Complex and Turbulent Flows, *Annu. Rev. Fluid Mech.* 45 (2013) 409–436. doi:10.1146/annurev-fluid-120710-101204.
- [58] F. Scarano, M.L. Riethmuller, Iterative multigrid approach in PIV image processing with discrete window offset, *Exp. Fluids.* 26 (1999) 513–523. doi:10.1007/s003480050318.
- [59] S. Shen, M. Jia, T. Wang, Q. Lü, K. Sun, Measurement of the droplets sizes of a flash boiling spray using an improved extended glare point velocimetry and sizing, *Exp. Fluids.* 57 (2016) 1–16. doi:10.1007/s00348-016-2147-3.
- [60] A.R. Glover, S.M. Skippon, R.D. Boyle, Interferometric laser imaging for droplet sizing: a method for droplet-size measurement in sparse spray systems, *Appl. Opt.* 34 (1995) 8409–8421. doi:Doi 10.1364/Ao.34.008409.
- [61] C.T. Crowe, J.D. Schwarzkopf, M. Sommerfeld, T. Yutaka, *Multiphase Flows with Droplets and Particles*, 2nd Editio, CRC Press, Boca Raton, 2011. doi:10.1201/b11103.
- [62] W.R.A. Goossens, Review of the empirical correlations for the drag coefficient of rigid spheres, *Powder Technol.* 352 (2019) 350–359. doi:10.1016/j.powtec.2019.04.075.

APPENDIX A. LIST OF TEST CASES

Case No.	Trace Particle	Temperature (°C)	Liquid Flow Rate (ml/min)	Inlet Pressure (psi)	Ambient Pressure (psi)	Pressure Drop Ratio (%)
1	Smoke	21.5	0	15.3	15	4
2		21.5	0	36.1	35	4
3		21.5	0	108.9	105	4
4	Smoke	21.5	0	15.0	15	2
5		21.5	0	35.4	35	2
6		21.5	0	106.8	105	2
7	Smoke	21.5	0	15.6	15	6
8		21.5	0	36.9	35	6
9		21.5	0	111.0	105	6
10	Water Droplet	21.5	4.7	15.3	15	4
11		21.5	24.4	15.3	15	4
12		21.5	39.2	15.3	15	4
13		21.5	54.7	15.3	15	4
14		21.5	91.0	15.3	15	4
15	Water Droplet	21.5	10.0	36.1	35	4
16		21.5	24.5	36.1	35	4
17		21.5	89.5	36.1	35	4
18	Water Droplet	21.5	90.7	36.1	35	4
19		21.5	113.5	36.1	35	4
20		21.5	148.2	36.1	35	4
21	Water Droplet	21.5	24.0	106.8	105	2
22		21.5	68.0	106.8	105	2
23		21.5	110.2	106.8	105	2
24	Water Droplet	21.5	22.0	107.8	105	3
25		21.5	79.0	107.8	105	3
26		21.5	24.0	108.9	105	4
27		21.5	90.0	108.9	105	4

APPENDIX B. SUMMARY OF MEASUREMENT RESULTS OF SPRAY FLOWS

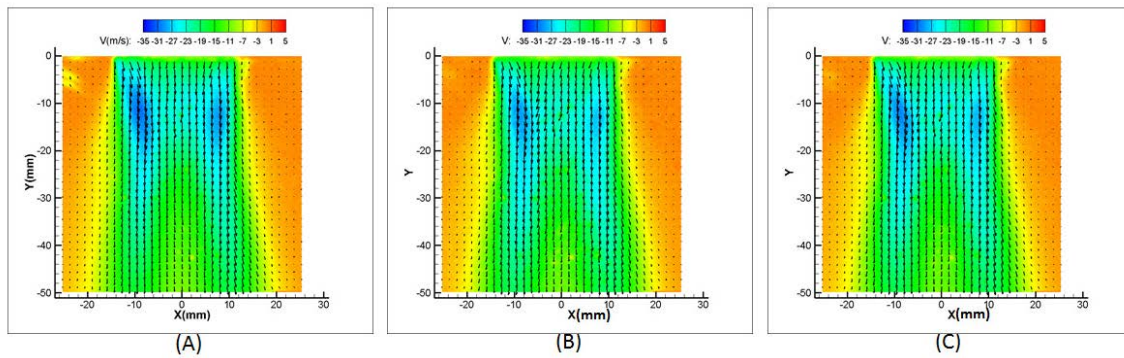


Figure B-1. Time-averaged velocity fields of spray flow at a pressure drop ratio of 2% with an ambient pressure 105 psi and flow rates of (a). 20 ml/min, 68 ml/min and (c). 110 ml/min.

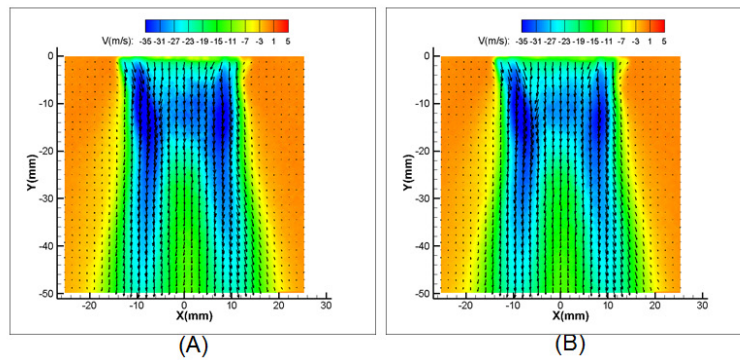


Figure B-2. Time-averaged velocity vector fields of spray flow at a pressure drop ratio of 3% with an ambient pressure 105 psi and liquid flow rates of (a). 22 ml/min and (b). 79 ml/min.

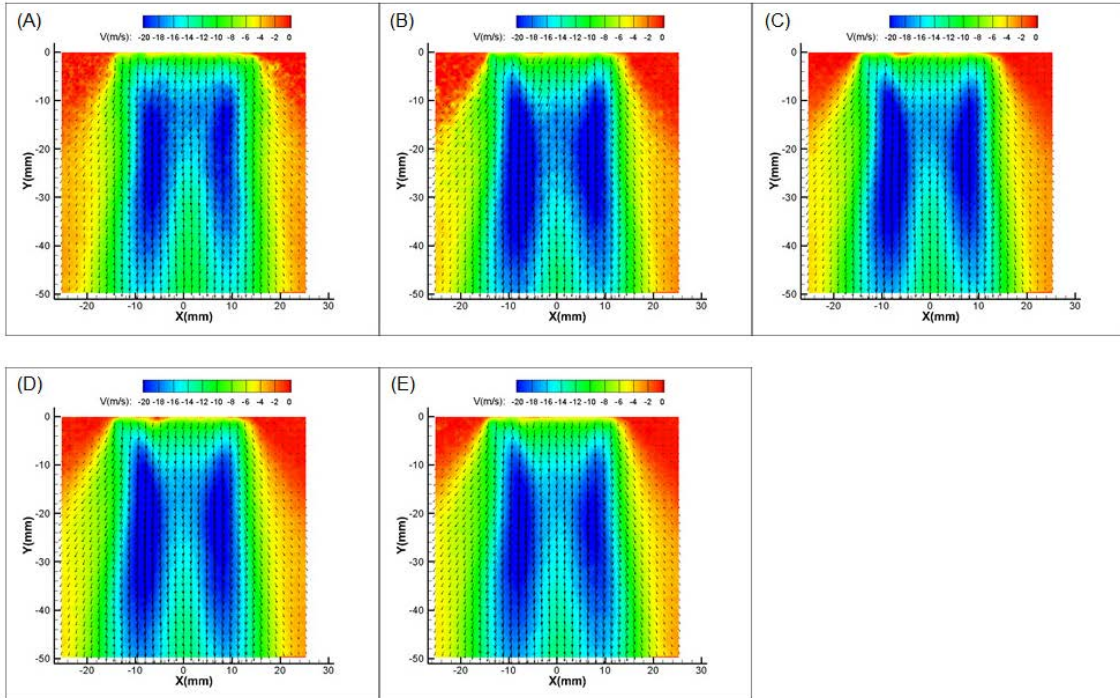


Figure B-3. Time-averaged velocity vector fields of spray flow at a pressure drop ratio of 4% with an ambient pressure 15 psi and liquid flow rates of (a). 4.7 ml/min, (b) 24.4 ml/min, (c) 39.2 ml/min, (d) 54.7 ml/min and (e). 91 ml/min.

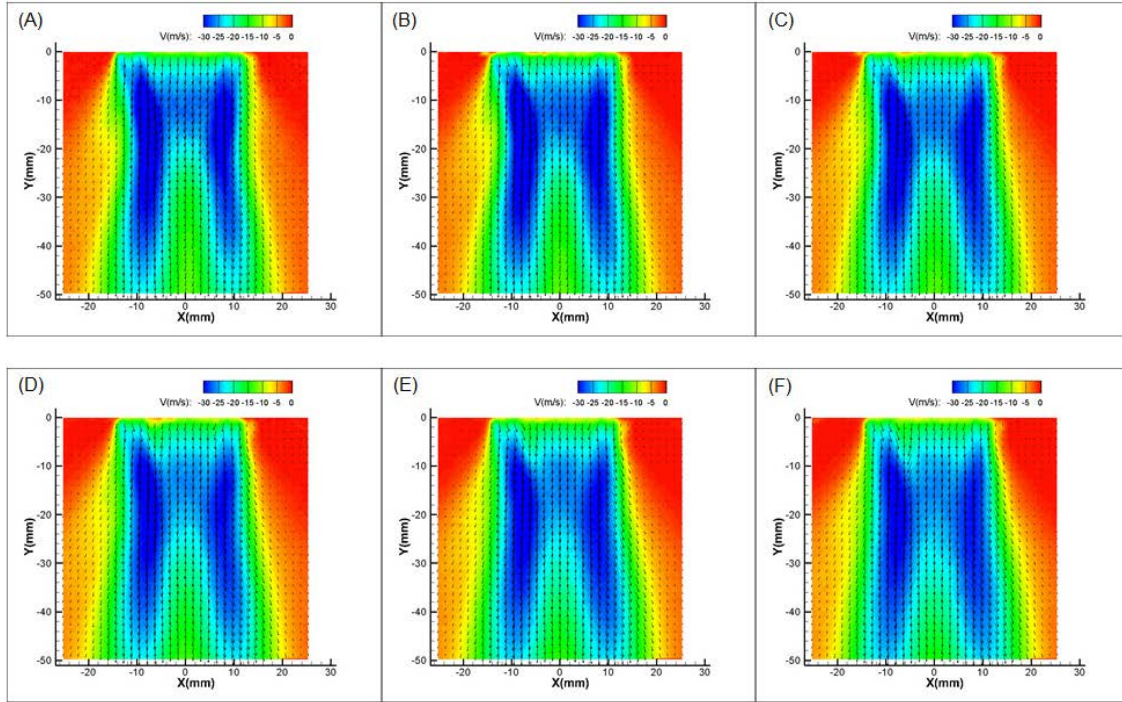


Figure B-4. Time-averaged velocity vector fields of spray flow at a pressure drop ratio of 4% with an ambient pressure 15 psi and liquid flow rates of (a). 10.0 ml/min, (b) 24.5 ml/min, (c) 69.5 ml/min, (d) 90.7 ml/min, (e). 113.5 ml/min and (f). 148.2 ml/min.